Acknowledgements

I would like to wholeheartedly thank everyone who has helped, encouraged and supported me during this diploma project.

First of all, I would like to thank my supervisor Dr. Andrey Danilov who was helping me every day, even in the weekend, holiday, and the evening. He is objective, patient, responsible, earnest, and humorous. He corrected my mistakes, and explained theory to me, and etc. He was teaching me how to do research, and how to be independent. The whole thesis project is under his supervision.

Many thanks to PhD students Sebastian De Graaf, Philip Krantz, Samuel Lara Avila for helping me with experiments, giving me training in the cleanroom, answering my questions almost every day. They are always very patient and give help whenever I want. I benefited a lot from discussions with them.

Lots of thanks to Dr. Thilo Bauch for helping me with measurements. Thank Prof. Sergey Kubatkin, Prof. Per Delsing, and Chris Wilson for nice discussions and encouragement and support.

Post Doc Kyle Sundqvist helped me with Mathematica. PhD student Seckin Kintas taught me quantum information theory, and Arsalan Pourkabirian, Io-Chun Hoi, Andre Dankert, Michael Simoen, Thomas Yager, Arseniy Lartsev, Shahid Nawaz, Simon Abay Gerbrehiwot, Wu Fan, etc. gave me training in the cleanroom and helped me with bonding…I really appreciate it.

Thank Erasmus program coordinator Prof. Guido Groeseneken for all the help and encouragement during my master's study.

Thank all members of MC2 for providing me with the friendly and international environment.

Finally, sincerely thank my parents for their strong support and encouragement. Thanks to my boyfriend Qing for being so understanding and thoughtful, encouraging me all the time and helping me to overcome any hardships.

Abstract

This diploma project is dedicated to fabrication of coplanar waveguide (CPW) Nb resonators on sapphire substrate for measurements on molecular spins. To achieve strong coupling between microwave field and molecular spins constrictions of the central conductor at the antinode of current were made to get local enhancement of magnetic field.

Simulations of resonators, T-junctions and constrictions which gave a good guideline of designs and fabrications were done. Low temperature measurements of resonators without (and with) local constrictions verified the accuracy of simulations. Temperature dependence and power dependence of transmission spectra for resonators without (and with) constrictions are discussed.

By fitting experimental data to theoretical formula deduced from lumped element equivalent circuit model, internal quality factor (Qint), external quality factor (Qext) and coupling capacitance (Ck) were evaluated. We achieve excellent agreement among simulations, measurements and theory. Qint of resonators without constrictions is ~ 100000 at ~1.5 K. Constrictions which introduce extra internal losses, and reduce Qint of the resonators to ~ 45000 at ~1.5 K. Qint of resonators with constrictions increases to ~ 70000 when temperature decreases to ~15 mK. Temperature dependence of resonance frequency could be well explained by kinetic inductance, giveing transition temperature (Tc) of Nb film of 10.67 K.

Hysteretic behaviour was observed for resonators without constrictions at high driving power due to nonlinear kinetic inductance. For resonators with constrictions, two hysteretic loops were observed.

Keywords: quantum information, CPW resonator, QED, superconductivity, microwaves, microwave devices, quantum optics

Contents

List of Figures

List of Tables

Symbols & Abbreviations

Abbreviations

QED	Quantum Electrodynamics
qubit	Quantum bit
QIP	Quantum information processing
CPW	Coplanar waveguide
TL	Transmission line
Q	Quality factor
Qint	Internal quality factor
Qext	External quality factor
PCB	Printed circuit board
DC	Direct current
Tc	Critical temperature
LHe	Liquid helium
LN2	Liquid nitrogen
EM	Electromagnetic
2D/ 3D	Two dimensions/ Three dimensions

Constants

e	Absolute value of electron charge
$\hbar$	Planck constant
c	Velocity of light in vacuum

Symbols

$\|\mathbf{0}\rangle, \|\mathbf{1}\rangle$	Ground state and first excited state
g	Qubit-photon coupling strength per single photon field
$\hat{a}$, $\hat{a}^{\dagger}$	Annihilation and creation operators of an LC-oscillator
Γ	Voltage reflection coefficient
$\mathbb{T}$	Voltage transmission coefficient
Q	Quality factor
Q_{int}	Internal quality factor
Q_{ext}	External quality factor
$\|\mathbf{\Psi}\rangle$	Wave function
m	Mass of a particle

1

Introduction

In this chapter, a short introduction to quantum computing and Cavity Quantum Electrodynamics will be presented. Then the goal of this thesis will be stated.

1.1 Quantum computing

Quantum computing originated from an article by Richard P. Feynman[1] back in 1982, in which he discussed about the 'possibility that there is to be an exact simulation, that the computer will do exactly the same as nature.'

The first difference between quantum computer and classical computer is the unit of information. Classical computer uses bit, which can take the value 0 or 1. While quantum computer takes quantum bit, which is called in short qubit, as the unit of information. Qubit can be in a superposition of states $|\mathbf{0}\rangle$ and $|\mathbf{1}\rangle$

$$\Psi = \alpha|\mathbf{0}\rangle + \beta|\mathbf{1}\rangle$$

Once a measurement is performed, the qubit state will collapse into either $|\mathbf{0}\rangle$ or $|\mathbf{1}\rangle$ with a certain possibility defined by $|\boldsymbol{\alpha}|^{\mathbf{2}}$ and $|\boldsymbol{\beta}|^{\mathbf{2}}$ respectively.

Secondly, in classical computers, the results are calculated from a series of fixed inputs. In quantum computers, the result of one calculation is just one of the possible results. Algorithm

is to maximize the possibility to collapse to the correct result. By running the algorithm repeatedly, the probability of getting the correct result is increased. More detailed discussion about the algorithm could be found from literature [2].

Furthermore, classical computers use transistors which manipulate charge on a capacitor to implement processors, and a collection of magnetic domains on a hard drive as non-volatile memory, while the elements of quantum computers span the range from microscopic systems, such as trapped ions and atoms and electron and nuclear spins, to mesoscopic circuits based on Josephson junctions. Spins which are naturally protected from decoherence due to weak coupling to the environments have long coherence times. So these microscopic systems are difficult to be read and manipulated, but they are good candidates for memory registers. On the other hand, Josephson junction quibts couple very strongly to external fields, and they have short coherence times. In this way, fast manipulation, readout and control are feasible for Josephson junction circuits. Then mesoscopic circuits are easier to be used as processors.

The advantages of quantum computers become obvious when factorization and discrete logarithms are involved. Also quantum computers are better at simulation of quantum physical process compared to classical computers. These advantages of quantum computers have led to the fast development of a new field of research, which combines physics and information science, the ‘quantum information’.

1.2 Cavity Quantum Electrodynamics

Cavity Quantum Electrodynamics (cavity-QED) based on quantum optics is the realization of thought experiments illustrating the basics laws of quantum physics. It deals with the information storage, transformation and readout between photons and qubits or between two qubits. Atom-photon interaction is a simple concept in theory, but it is difficult to be implemented in the labs. To minimize the perturbations from environment, an atom is isolated in a cavity with high reflecting walls. The field is quantized in the cavity as a set of harmonic oscillators with different resonance frequencies, which could be easy tuned by adjusting walls. In this way, atom-photon interaction could be tuned by macroscopic mirrors.

In 1985 spontaneous emission enhancement by a resonant circuit was observed by Feher et al. [3] in the NMR experiment. A more quantitative research of the effect of a cavity had been

done when Rydberg atoms were studied in 1982 by Raimond et al [4]. Strong coupling regime is reached when the atom-field interaction rates exceeds dissipation rates. Coupling strength of an ensemble of N atoms is enhanced by $\sqrt{N}$ [5, 6, 7]. So strong coupling regime could be reached if

$$g\sqrt{N} \gg \boldsymbol{\kappa, \gamma,}$$

where g is the coupling strength of an individual atom, and κ and γ are the resonator and atom damping rates. The trapping of microwave photons in very high-Q superconducting cavities has led to a breakthrough in Cavity-QED, and brings large improvement over the Rydberg atom experiments described above.

In 2010, in Physical Review Letters, experiments demonstrating the coupling of superconducting CPW resonators to spin ensembles containing ~10^{12} electron spins have been reported by two groups [8, 9]. These experiments show exchange of microwave photons between the resonator and the spin ensemble, which is evident in an observed vacuum Rabi splitting.

1.3 Thesis goal

Quantum information processing (QIP) concerns communication between qubits in quantum computer. So far coplanar waveguide CPW resonators were used to arrange communication between Josephson qubits which have relatively short coherence times. The qubits based on molecular spins maintain quantum coherence for much longer time, but they have too weak coupling to microwave field to allow effective spin manipulation. This project is to optimize CPW resonators to obtain strong coupling to molecular spins and to explore the coupling principle between photons and spins.

In transmission line (TL) resonators, current flows along edges of central conductor and ground plane. The goal of this project is to make constrictions at the antinode of the current, such as in the center of the resonator in this project, to increase current density, and therefore locally increase the magnetic field. The objective of this master diploma project is to make simulations, design, fabrication and low-temperature measurements in order to prepare these resonators with high Qs for measurements on molecular spins.

2

Theoretical background

The basic theory involved in this project will be described in this chapter. This includes field quantization, CPW resonators, and spin-spring interaction.

2.1 Field quantization

Electromagnetic field confined in a one-dimensional cavity, as shown in figure 2.1, should satisfy Maxwell's equation and boundary conditions.

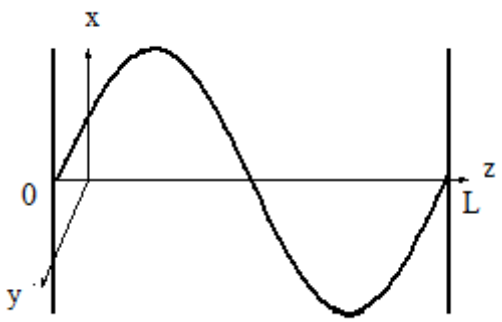

Figure 2.1 Cavity with perfectly conducting walls at z=0 and z=L. Electromagnetic field is confined inside.

If there are no sources of radiation, and the field is assumed to be polarized along the x-direction. A single-mode field is given by

$$E(r,t) = e_x E_x(z,t) \qquad (1)$$

$$E_x(z,t) = (\frac{2\omega^2}{V\varepsilon_0})^{1/2} q(t)\sin(kz) \qquad (2)$$

$$B(r,t) = e_y B_y(z,t) \qquad (3)$$

$$B_y(z,t) = (\frac{\mu_0\varepsilon_0}{k})(\frac{2\omega^2}{V\varepsilon_0})^{1/2} \dot{q}(t)\cos(kz) \qquad (4)$$

Where e_x and e_y are unit polarization vectors, ω is the frequency of the mode and k is the wave number, V is the effective volume of the cavity. The boundary conditions E(z)=0 at z=0 and z=L make the allowed frequencies quantized. Assume ω is one of these frequencies. q(t) is a time-dependent factor having the dimension of length, and

$$p(t) = \dot{q}(t)$$

In classical field energy (Hamiltonian H) of the single-mode field is given by

$$H = \frac{1}{2}\int dV[\varepsilon_0 E^2(r,t) + \frac{1}{\mu_0} B^2(r,t)]$$

Which, after substitution of equations (1, 2, 3, 4), transfers into

$$H = \frac{1}{2}(p^2 + \omega^2 q^2)$$

This shows that a single-mode field is equivalent to a harmonic oscillator of unit mass, where the electric and magnetic fields act as canonical position and momentum.

Replace canonical variables q and p by operator $\hat{q}$ and $\hat{p}$, then the Hamiltonian becomes

$$\hat{H} = \frac{1}{2}(\hat{p}^2 + \omega^2 \hat{q}^2)$$

$\hat{q}$ and $\hat{p}$ are Hermitian and correspond to observables. Follow the secondary quantization technique, annihilation ($\hat{a}$) and creation ($\hat{a}^{\dagger}$) operators could be introduced. As a result, Hamiltonian takes the form $\hat{H} = \hbar\omega(\hat{a}^{\dagger}\hat{a} + \frac{1}{2})$. More information could be found from reference [10].

2.2 CPW Resonator

A coplanar waveguide (CPW) resonator (Figure 2.2) is a distributed device with voltages and currents varying in magnitude and phase over its length. Superconducting CPW resonators are widely used in cavity-QED. First of all, CPW resonators can easily be designed and fabricated to operate at frequencies up to 10 GHz. Compared with lumped element resonators, they have better microwave properties. Also the impedance of CPWs can be controlled easier (for example, by tuning lateral size) than other distributed element resonators, such as microstrip line resonators. Furthermore, the potentially small lateral dimension of CPWs allows obtaining large vacuum fields due to small mode volume [11]. In this project, superconducting CPW resonators are used as the cavity to trap photons, and two capacitors at both ends act as mirrors. Moreover, CPW resonators with large internal quality factor (up to several hundred thousand) could be routinely realized [12, 13, 14].

A resonator is characterized by its resonance frequency and quality factor Q. Resonance frequency is the frequency at which the stored energy oscillates between capacitor and inductor without external excitation. Q-value describes the rate of energy loss with respect to the stored energy and is defined as $\mathrm{Q} = 2\pi \frac{\text{Energy stored}}{\text{Energy loss per cycle}}$. $\mathrm{Q_{int}}$ characterises the internal losses in a resonator, and $\mathrm{Q_{ext}}$ stands for external losses due to external coupling to feedlines, and

$$\frac{1}{\mathrm{Q_{tot}}} = \frac{1}{\mathrm{Q_{ext}}} + \frac{1}{\mathrm{Q_{int}}}.$$

CPW resonator is a section of TL. The distributed element representation of TL is in figure 2.2b. For a piece of TL,

$$Z_0 = \sqrt{\frac{R_{pul} + i\,\omega\,L_{pul}}{G_{pul} + i\,\omega\,C_{pul}}}$$

$$\gamma = \alpha + i\,\beta = \sqrt{(R_{pul} + i\,\omega\,L_{pul})(G_{pul} + i\,\omega\,C_{pul})} v_p = \frac{\omega}{\beta}$$

Z_0 is characteristic impedance; γ is complex propagation constant; α is attenuation constant; v_p is phase velocity, β is phase constant. For lossless line, $R_{pul} = G_{pul} = 0$. $Z_0 = \sqrt{\frac{L_{pul}}{C_{pul}}}$, $v_p = \frac{1}{\sqrt{L_{pul}\,C_{pul}}} = \frac{c}{\sqrt{\epsilon_{eff}}}$, where ϵ_{eff} is the effective permittivity of the CPW substrate, and it is a function of the geometry, such as crystal orientation, and relative permittivity ϵ_1.

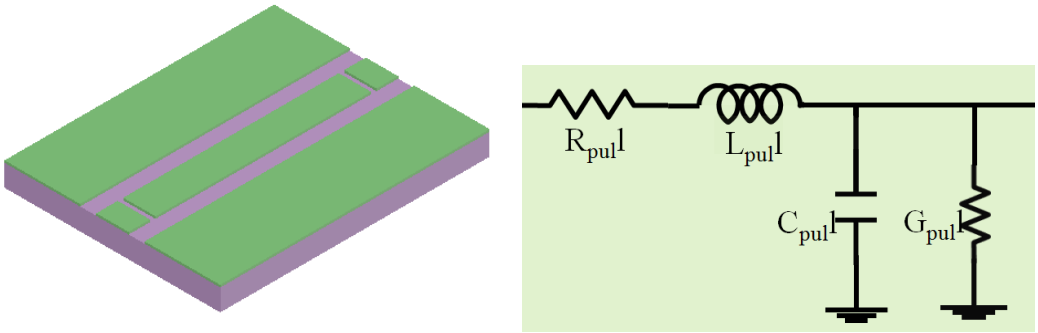

(a) (b)

Figure 2.2 (a) schematics of CPW resonator; (b) distributed element representation of TL. R_{pul}: Series resistance per unit length, in Ω/m, L_{pul}: Series inductance per unit length, in H/m, G_{pul}: Shunt conductance per unit length, in S/m, C_{pul}: Shunt capacitance per unit length, in F/m

For small coupling capacitors, as is the case in this project, the frequency shift induced by coupling can be neglected. So the resonator's fundamental frequency f_0 [15] is given by

$$f_0 = \frac{c}{\sqrt{\epsilon_{eff}}}\,\frac{1}{2\,l}$$

Circuit model used in this project will be discussed in more detail in section 7.1.

2.3 Spin-spring interaction

The coupling of a two-level system which is modelled as a spin, with a quantum harmonic oscillator will be considered in this section. The description below is cited mainly from reference [10].

In the absence of external fields, the Hamiltonian of an electron bound to an atom is

$$\hat{H}_0 = \frac{1}{2\,m}\,\hat{\mathbf{p}}^2 + V(r)$$

V(r) is the Coulomb interaction; $r = |\boldsymbol{r}|$, $\hat{\boldsymbol{p}} = -i\,\nabla$

Within the dipole approximation, in the presence of external fields, the Hamiltonian is

$$\hat{H}' = \hat{H}_0 - \hat{\boldsymbol{d}} \bullet \mathbf{E}(\mathrm{t})$$

$\hat{\boldsymbol{d}} = -e\,\boldsymbol{r} = -|\boldsymbol{e}|\,\boldsymbol{r}$ is dipole moment,

The discussion above is valid for both classical field and quantum mechanical field.

2.3.1 The Rabi model

When a strong laser field has frequency near resonance with two atomic levels (figure 2.3), a large population transfer will happen to the near resonant state, but not to any other. In this case, the Rabi model could be used to solve the problem.

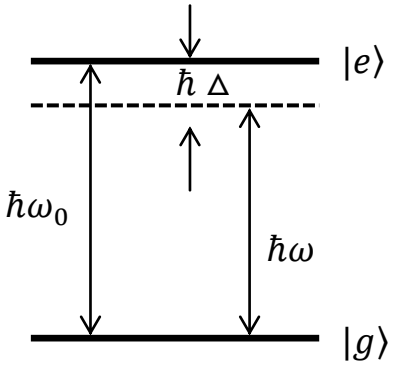

Figure 2.3: Energy level diagram for a two-level atom interacting with a near resonant classical driving field. The energy difference between excited state and ground state is $\hbar\omega_0$. The frequency of the driving field is ω. The detuning is $\Delta = \omega_0 - \omega$.

The interaction Hamiltonian is

$$\widehat{H}^{(\mathrm{I})}(t) = -\widehat{\boldsymbol{d}} \cdot \boldsymbol{E}_0 \cos \omega t$$

With the state vector as

$$|\psi(t)\rangle = C_g(t)e^{-i\,E_g\frac{t}{\hbar}}|g\rangle + C_e(t)e^{-i\,E_e\frac{t}{\hbar}}|e\rangle$$

and an initial condition $C_g(0) = 1$ and $C_e(0) = 0$ solve the Schrödinger equation

$$i\,\hbar\,\frac{\partial|\psi(t)\rangle}{\partial t} = \widehat{H}(t)|\psi(t)\rangle$$

Then the solution is

$$\mathrm{C_e(t)} = \mathrm{i}\frac{\langle \mathrm{e}|-\hat{\mathbf{d}}\cdot\mathbf{E_0}|\mathrm{g}\rangle}{\Omega_\mathrm{R}\hbar}\,\mathrm{e}^{\mathrm{i}\Delta\mathrm{t}/2}\sin\left(\Omega_\mathrm{R}\mathrm{t}/2\right)$$

$$\mathrm{C_g(t)} = \mathrm{e}^{-\mathrm{i}\Delta\mathrm{t}/2}\left[\frac{\mathrm{i}\Delta\sin\left(\frac{\Omega_\mathrm{R}\mathrm{t}}{2}\right)}{\Omega_\mathrm{R}} + \cos\left(\frac{\Omega_\mathrm{R}\mathrm{t}}{2}\right)\right]$$

Where Ω_R is Rabi frequency. $\Omega_\mathrm{R} = (\Delta^2 + \frac{\langle \mathrm{e}|-\hat{\mathbf{d}}\cdot\mathbf{E_0}|\mathrm{g}\rangle^2}{\hbar^2})^{1/2}$

If $\Delta = 0$, atomic inversion which is the difference between the excited and ground state population becomes $\mathrm{W(t)} = \left|\mathrm{C_g(t)}\right|^2 - |\mathrm{C_e(t)}|^2 = \cos\left(\langle \mathrm{e}|-\hat{\mathbf{d}}\cdot\mathbf{E_0}|\mathrm{g}\rangle \mathrm{t}/\hbar\right)$.

2.3.2 The Jaynes-Cummings model

The Jaynes-Cummings model is quantum electrodynamic version of the Rabi model. Consider the same situation as figure 2.3. The single-mode cavity field is

$$\hat{E} = \boldsymbol{e}\left(\frac{\hbar\omega}{\varepsilon_0 V}\right)^{1/2}\left(\hat{a} + \hat{a}^\dagger\right)\sin(kz) = -\boldsymbol{e}g\left(\hat{a} + \hat{a}^\dagger\right)$$

Where **e** is an arbitrarily oriented polarization vector, $g = -\left(\frac{\hbar\omega}{\varepsilon_0 V}\right)^{1/2}\sin(kz)$

Then the interaction Hamiltonian is

$$\hat{H}^{(\mathrm{I})}(t) = \hbar\lambda(\hat{\sigma}_+ + \hat{\sigma}_-)(\hat{a} + \hat{a}^\dagger)$$

Where $\lambda = \frac{dg}{\hbar} = \frac{\langle e|\hat{d}|g\rangle g}{\hbar}$, $\hat{\sigma}_+ = |e\rangle\langle g|$ and $\hat{\sigma}_- = |g\rangle\langle e|$ are atomic transition operators.

Making the rotating wave approximation (RWA), the Hamiltonian describing the system is

$$\hat{H}(t) = \frac{1}{2}\hbar\omega_0\hat{\sigma}_3 + \hbar\omega\hat{a}^\dagger\hat{a} + \hbar\lambda(\hat{\sigma}_+\hat{a} + \hat{\sigma}_-\hat{a}^\dagger)$$

and $\hat{\sigma}_3 = |e\rangle\langle e| - |g\rangle\langle g|$ is the inversion operator.

Consider a simple example when $\Delta = 0$ and initial condition is $C_g(0) = 1$ and $C_e(0) = 0$.

If the field is initially in the number state $|\mathrm{n}\rangle$, then the atomic inversion $\mathrm{W(t)} = \left|\mathrm{C_g(t)}\right|^2 - |\mathrm{C_e(t)}|^2 = \cos\left(2\lambda\mathrm{t}\sqrt{\mathrm{n}+1}\right)$ and the Rabi frequency $\Omega_\mathrm{R} = 2\lambda\sqrt{\mathrm{n}+1}$.

If the field is initially in the coherent state, which is the 'most classical' quantum states of a harmonic oscillator,

$|\psi(0)\rangle_{\text{field}} = \sum_{\mathrm{n}=0}^{\infty} \mathrm{e}^{-|\alpha|^2/2}\frac{\alpha^\mathrm{n}}{\sqrt{\mathrm{n}!}}|\mathrm{n}\rangle$, then $\mathrm{W(t)} = \mathrm{e}^{-|\alpha|^2}\sum_{\mathrm{n}=0}^{\infty}\frac{|\alpha|^{2\mathrm{n}}}{\mathrm{n}!}\cos\left(2\lambda\mathrm{t}\sqrt{\mathrm{n}+1}\right)$ (Figure 2).

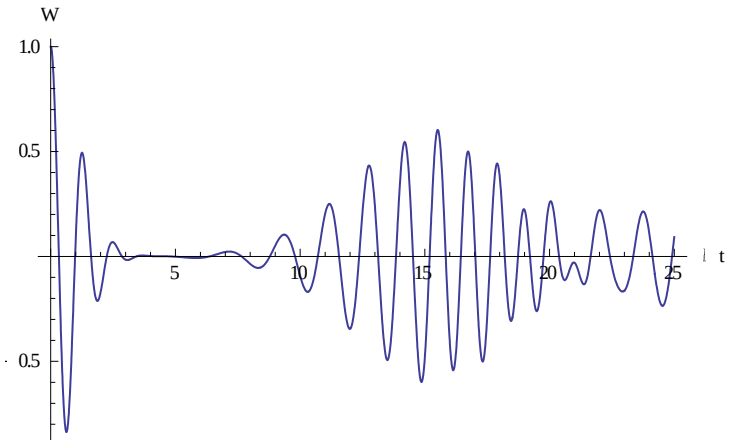

Figure 2.4 Atomic inversion with the field initially in a coherent state $|\alpha|^2$=5.

3

Simulations and Design

Prior to fabrication and measurement, simulation is crucial to give a prediction of the properties of devices. This chapter is dedicated to describe the simulations that were done during this project. In the end, the design of the chip is discussed.

3.1 Simulations

Simulations in this project are divided into three parts. The first part is the basic simulation of resonators which will give the relation between physical parameters and electrical parameters. The second part is T-junction which is used to connect resonators with feedlines. The third part is simulations of local constrictions with enhanced magnetic field.

3.1.1 Key parameters of the resonators

3.1.1.1 Simulation with AWR Design Environment

The simulations in this project were done with AWR Design Environment. The resonators are $\lambda/2$ CPW resonators with resonance frequency around 6 GHz. Open-circuit $\lambda/2$ transmission line resonators are coupled to external circuit via coupling capacitors. At resonance, electrical field has maximum at two ends and magnetic field gets maximal in the center. Since the

ultimate goal of this project is to make constrictions in the center of resonators to increase magnetic field locally, we want the width of central conductor to be as small as possible.

Physical and electrical parameters used during the simulations are listed in table 1. Since the loss tangent of substrate is zero and metal resistivity is zero, the Q_{int} is infinite. Then $Q_{tot} = Q_{ext}$.

Table 3.1: Parameters used during simulation

Substrate relative dielectric constant	9.8
Substrate thickness	380 um
Substrate loss tangent	0
conductor thichness	200 nm
conductor bulk resistivity nomalized to gold	1.00E-15
Accuracy parameter(Acc)	10

Modelling schematic is shown in figure 3.1(a). Two sets of resonators were simulated, one for photolithography, and one for electron beam lithography. The goal of simulations is to get resonators with Q from 10000 to 300000. The element in the middle is a $\lambda/2$ transmission line resonator, the EM structures on both sides represent coupling capacitors. Two ports on two ends stand for feedline through which we excite and measure resonators. Dimensions of CPW TL (figure 3.1(b)) and the shape of the EM coupling capacitor (figure 3.1(c, d)) corresponding to desired Qs are to be determined. The simulation results are listed in table 3.2 and table 3.3. Resonators for photolithography have minimum dimension 2 um, while the minimum dimension of resonators for electron beam lithography is 400 nm. The length of TL resonator determines resonance frequency, while the coupling capacitor gives Q. Different combination of W and S should give a characteristic impedance of TL $Z_0 = 50\ \Omega$.

Because time is limited in this project, only the five resonators which are listed in table 3.2 were fabricated and measured.

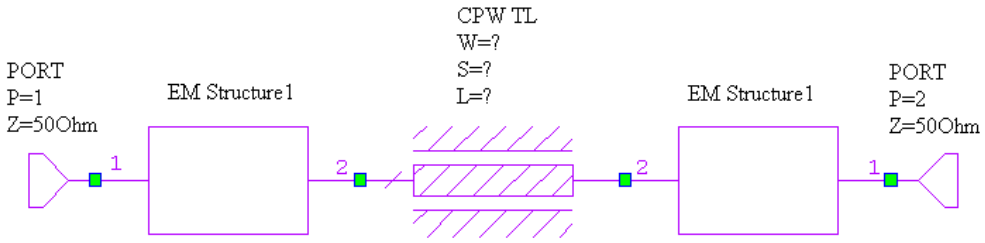

(a)

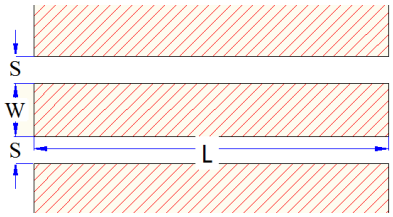

(b)

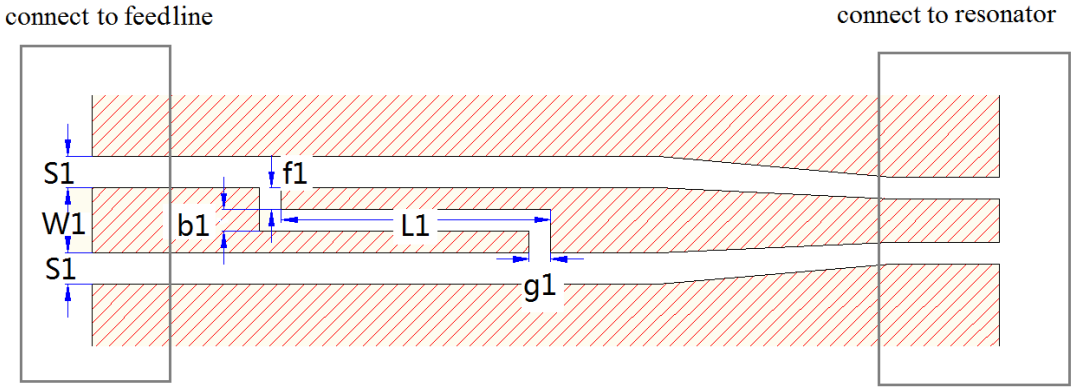

(c)

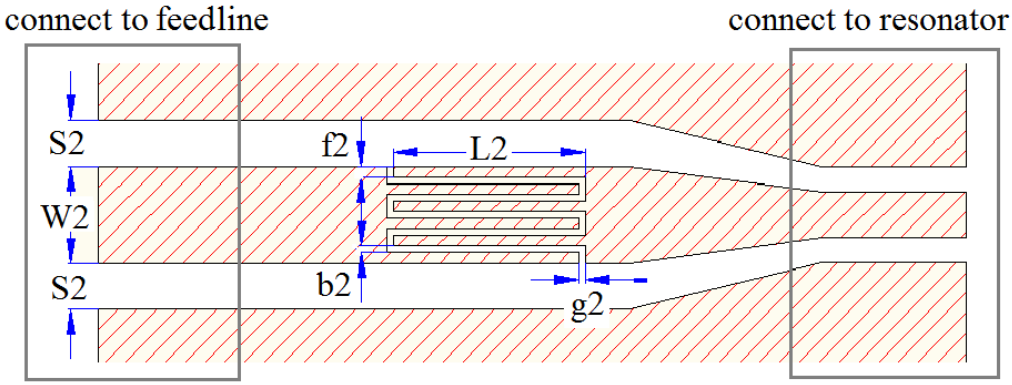

(d)

Figure 3.1 (a) Schematics of simulation model. TL resonator is shown in (b). The coupling capacitors for photolithography and electron beam lithography on the left side of resonator are shown in (c) and (d) respectively. Hatched area indicates metal, and drawings are not to the scale.

Table 3.2 Resonators for photolithography

number	S=2 um, W=4 um, S1=2.9 um, W1=6 um (One finger on each side)						
	resonance frequency		coupling capacitor				
	f0/GHz	L/um	Q	f1/um	L1/um	b1/um	g1/um
#1	6.1849	10541	2.60E+04	2	90	2	2
#2	6.0854	10762	5.80E+04	2	60	2	2
#3	5.9859	10975	1.27E+05	2	40	2	2
#4	5.8863	11178	2.21E+05	2	30	2	2
#5	5.7867	11380	3.13E+05	2	25	2	2

Table 3.3 Resonators for electron-beam lithography

Number	S=1.5um, W=2.8um,m: number of fingers on the feedline side, m': number of fingers on the resonator side									
	resonance frequency		coupling capacitor							
	f0/GHz	L/um	Q	f2/um	L2/um	b2/um	g2/um	m+m'	S2/um	W2/um
#1	5.7	11753	3.28E+05	1.2	15	0.4	0.4	1+1	1.5	2.8
#2	5.8	11559	3.27E+05	0.4	8	0.4	0.4	2+2	1.5	2.8
#3	5.9	11352	1.48E+05	0.4	12	0.4	0.4	2+2	1.5	2.8
#4	6	11113	4.94E+04	0.65	12	0.4	0.4	3+2	2.35	4.85
#5	6.1	10911	3.00E+04	0.65	12	0.4	0.4	3+3	2.8	5.9
#6	6.2	10704	1.28E+04	0.65	12	0.4	0.4	4+4	3.7	8

3.1.2 T-junction

T-junctions are used to connect the five selected resonators to a common feedline. In figure 3.2(a), port 1 and 2 are connected to feedline, and port 3 is connected with coupling capacitor. Because T-junction breaks the translational symmetry of the feedline, unexpected reflection and transmission could be introduced. In order to check the reflection and transmission at T-junctions, a simulation was done with the model in figure 3.3(a), and the results are shown in figure 3.3(b).

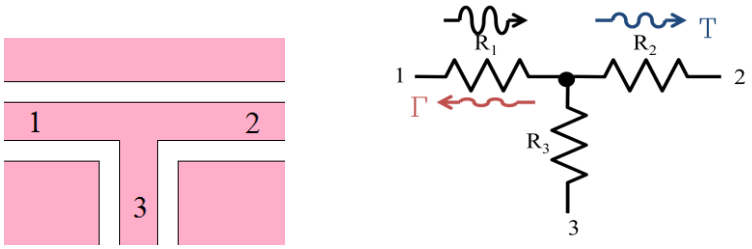

(a) (b)

Figure 3.2 (a) T-junction. Pink indicates metal. (b) Circuit model of T-junction. Γ is voltage reflection coefficient and T is transmission coefficient.

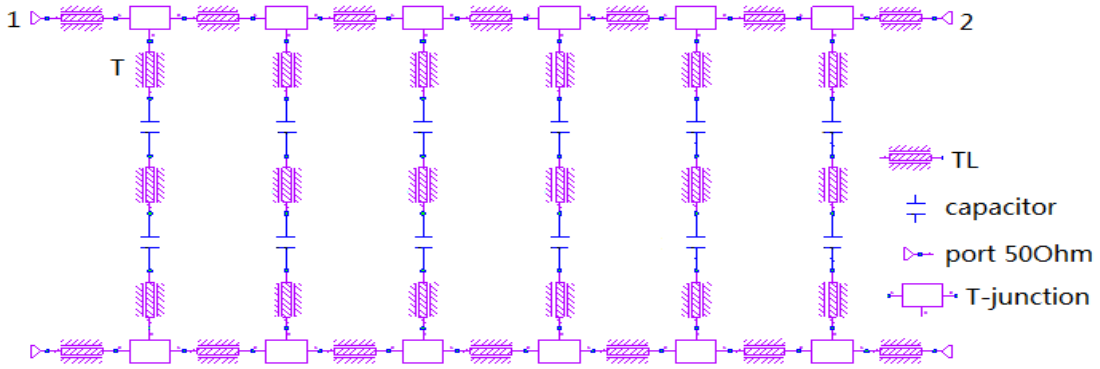

(a)

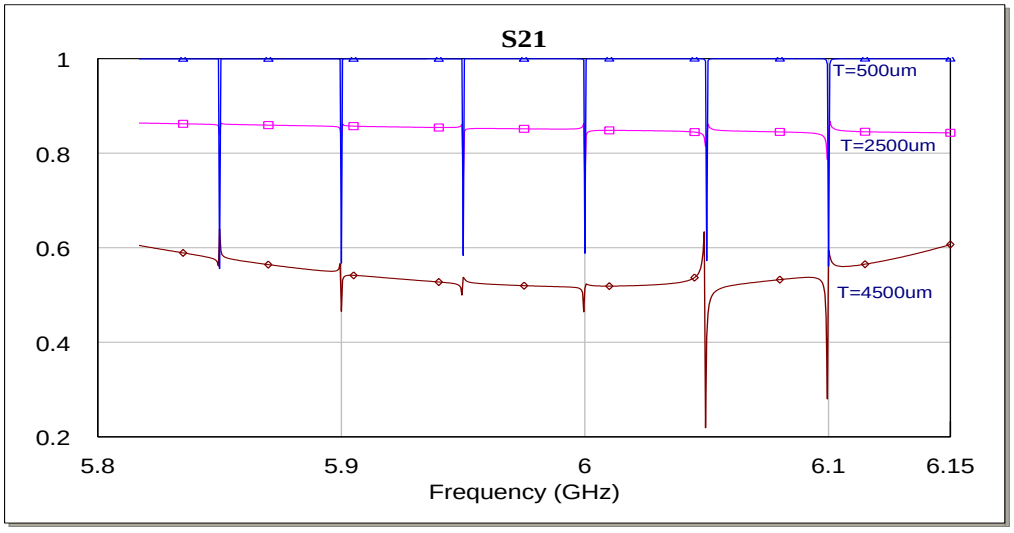

(b)

Figure 3.3 (a) Simulation model. 6 resonators have different resonance frequencies. T is the length of extension of feedline to resonators. (b) gives the transmission from port 1 to port 2(S21) when T is 500um, 2500um and 4500um.

The simulation results show that, if the extension of the feedline (T) is short, there is no extra reflection or transmission. When T is long enough, the three ports of T-junction could be

represented as circuit model as in figure 3.2(b) with $R_i = 50\Omega$ $(i = 1, 2, 3)$. So $S21 = T = \frac{2(\frac{R_2R_3}{R_2+R_3})}{\frac{R_2R_3}{R_2+R_3}+R_1} = \frac{2}{3}$. The background transmission has maximal value which is 2/3.

3.1.3 Resonators with constrictions

When we make constrictions in the center of resonators, the question is if the resonator will be split into two. Figure 3.4 and 3.5 depict simulations which are dedicated to answer this question. The model in figure 3.4(a) is used to simulate the effect of different constrictions on the resonance frequency and Q-value of the original resonator. The schematic and dimensions of constriction are shown in figure 3.4(b), and figure 3.5(a) gives simulation results. Figure 3.5(b) describes the current density distribution around the constriction (200 nm) at resonance frequency.

From simulation results, two conclusions could be reached. First of all, resonance frequency is shifted to lower value by constrictions of central conductor in the middle of resonator, while there is no obvious change with the Q-value. Second, the current density is enhanced by constrictions. Currents along two edges of central conductor combine together, when the central conductor gets narrower.

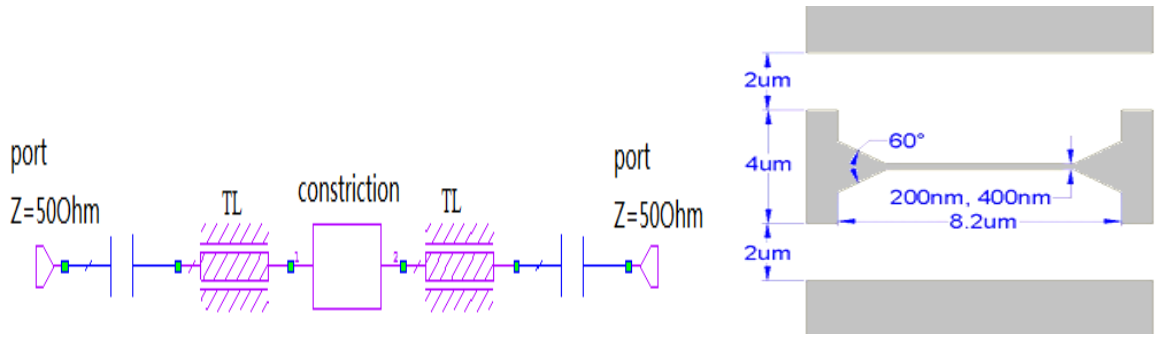

(a) (b)

Figure 3.4 (a) Constriction simulation model; (b) Schematic and dimensions of the constriction (gray indicates metal);

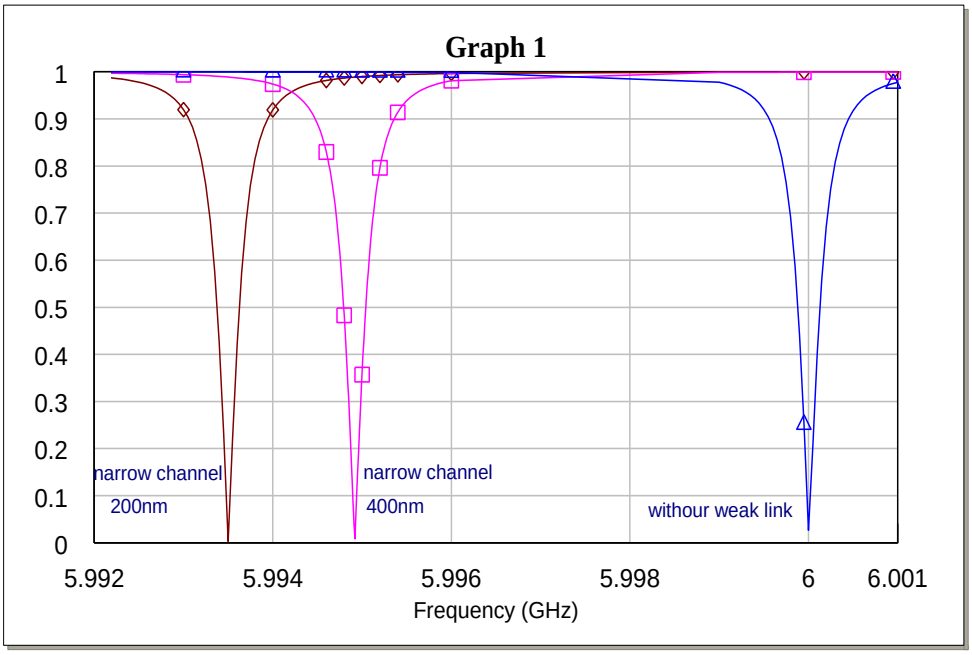

(a)

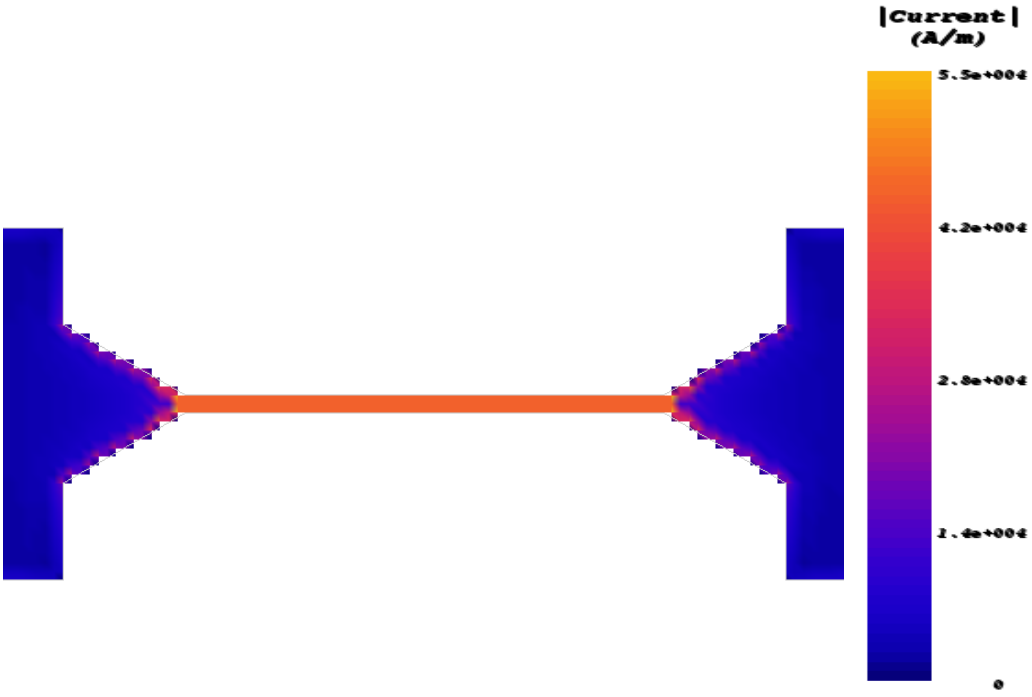

(b)

Figure 3.5 (a) Simulation results of resonator without constriction, and with constrictions (200 nm and 400 nm); (b) Current density distribution on the central conductor in the middle of resonator at resonance.

3.2 Sample design

After we got all the simulation results above, the design of the chip (10 mm×10 mm) was determined. In this project, only the set of resonators for photolithography was fabricated and measured. Therefore, only the design of chip for photolithography is discussed below. The pattern is drawn in AutoCAD. First of all, in order to increase measurement efficiency, five resonators which have different resonance frequencies and Q-values are implemented on one chip. Second, the TL is meandered to save space. Additionally, the distance of adjacent TL should be at least 10 times larger than W+2S to reduce parasitic coupling. To reduce reflection in the curved part, the radius of curvature should be at least 7 times larger than W.

Coupling capacitors are connected with feedline with T-junctions. The ends of feedline are widened (preserving the impedance) to have enough room (200 um×200 um) for two bondings. There is more than 1 mm open space around the chip, and 8 chip alignment markers for whole chip alignment and 4 constriction alignment markers near the centre of each resonator for future processing of local constrictions. At last, dicing markers are at four edges of the chip. The chip design, and optical microscope zoom in image of T-junction and coupling capacitor are shown in figure 3.6. Constrictions in the centre of each resonator will be discussed later.

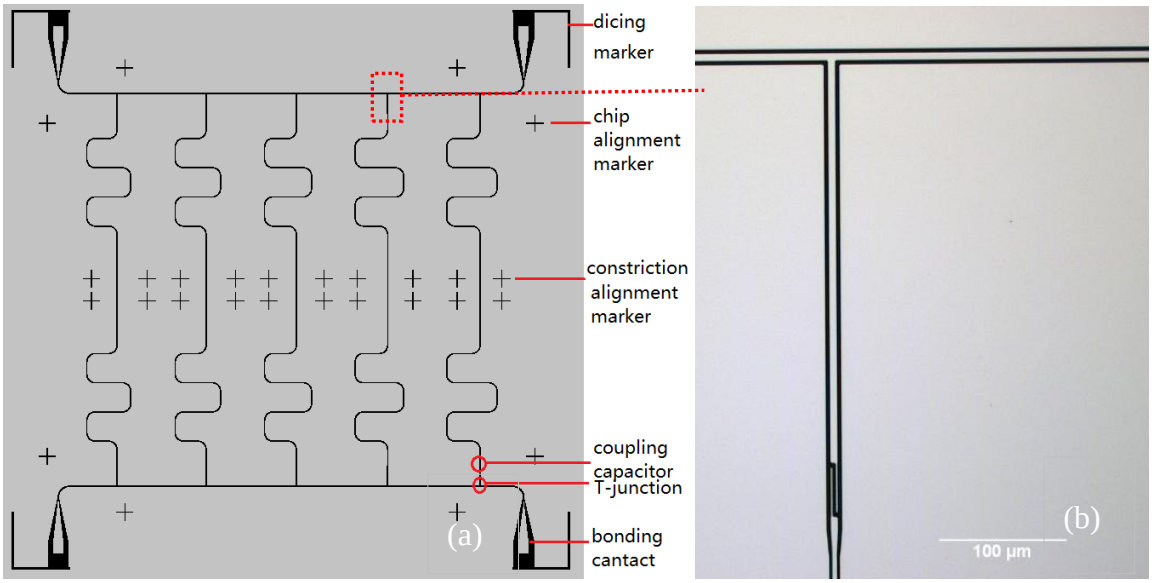

Figure 3.6 (a) Design of the chip. (b) Zoom in optical microscopy image of T-junction and coupling capacitor.

4

Fabrications

The fabrication processes will be discussed in this chapter. First of all, resonators without constrictions were fabricated with photolithography. Then constrictions were made with electron beam lithography. Discussion mainly covers description of the chip, electron beam lithography dose test and fabrication steps for constrictions.

4.1 Resonators without constrictions

The mask for optical lithography was produced in the cleanroom at Chalmers University of Technology by Lai Zonghe. The chips with Nb resonators (without constrictions) were ordered from STAR Cryoelectronics LLC, USA. The material and fabrication steps are interpreted in figure 4.1.

First of all, a layer of Nb (200 nm thcickness) is deposited on a 2'' sapphire wafer which has C-plane direction. Then a layer of photoresist which is a kind of light sensitive polymer is deposited. The resist is exposed by photolithography, and will be developed in next step. After developing, Nb without resist on top is removed by ion mill etching. Now the Nb on sapphire substrate has opening gaps. Before dicing, a layer of photoresist is deposited again to protect the patterns from particles generated during dicing. Then the wafer with Nb

resonators are put up-side-down on a piece of dicing tape, and dicing is done from the back side. In the end, after rinsing the resist, 8 complete chips are obtained.

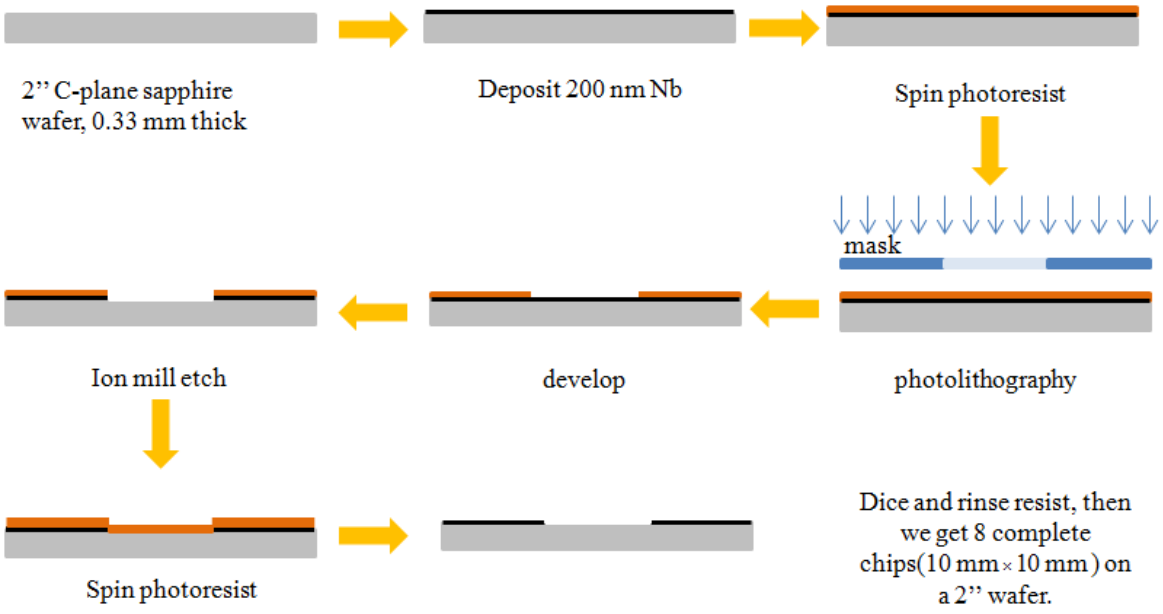

Figure 4.1 Fabrication of resonators without constriction.

4.2 Electron beam lithography dose test

The constrictions with the 200 nm narrow channel were made with electron beam lithography. The actual dimension depends not only on the resolution of electron beam machine, but also on a lot of other parameters, such as the resist thickness and property, development time, developer, and etch parameter, and etc. To find a suitable combination of all these parameters, electron beam lithography dose test is necessary.

Dose test and constriction fabrication were done by PhD student Sebastian De Draaf, and I did some simple operations under his supervision.

A sequential description of dose test process is shown in figure 4.2.

Figure 4.2 E-beam dose test and constrictions fabrication steps.

Because resonator circuit is not connected with outside and sapphire substrate is not conductive, during electron beam lithography and plasma etch charges will be collected on the central strips of resonators. To reduce this charge effect, first of all, 60 nm Al layer is deposited in Plassys with deposition speed of 5 A/second. Then a layer of zep520A is deposited with spinner with rotation speed of 3000 rpm. The solvent is removed by baking at 170º for 5 minutes. To get thick photoresist, zep520A are deposited twice. The thick resist is needed because in the following step - plasma etch, part of the photoresist will be removed. The next step is electron beam lithography with 2 nA current. 30 arrays of patterns which are the complementary patterns of 500 nm constriction are exposed at the ground plane of the chip with different electron beam doses. Then the zep520A is removed by oxylene for 30 s, rinsed immediately in isopropanol. Cl_2 plasma is used to etch away Al for 3 minutes and 10 seconds, and CF_4 plasma is used to etch away Nb for 3 minutes and 55 seconds. (Detail recipe could be found from appendix.) Then keep the chip in 1165 remover overnight to remove photoresist. The last step is to remove Al with MF319 developer for 5 minutes.

After electron-dose test, electron-beam dose of 395 uC/cm2 was chosen while keeping the other recipes the same.

4.3 Resonators with constrictions

Alignment is very important for electron beam lithography. Two of the chip alignment markers are used to align the whole chip, and constriction alignment markers are used to

align individual structure to make constrictions. Following the same fabrication procedures as in figure 4.2 and with electron beam dose of 395 uC/cm2 constrictions of the central conductor are made in the middle of each resonator. The SEM images of one of the constrictions are shown in figure 4.3. There is some Al (or Nb) residual left along the edges of central conductor. To make clean and well defined constrictions focused ion beam is worthy to try.

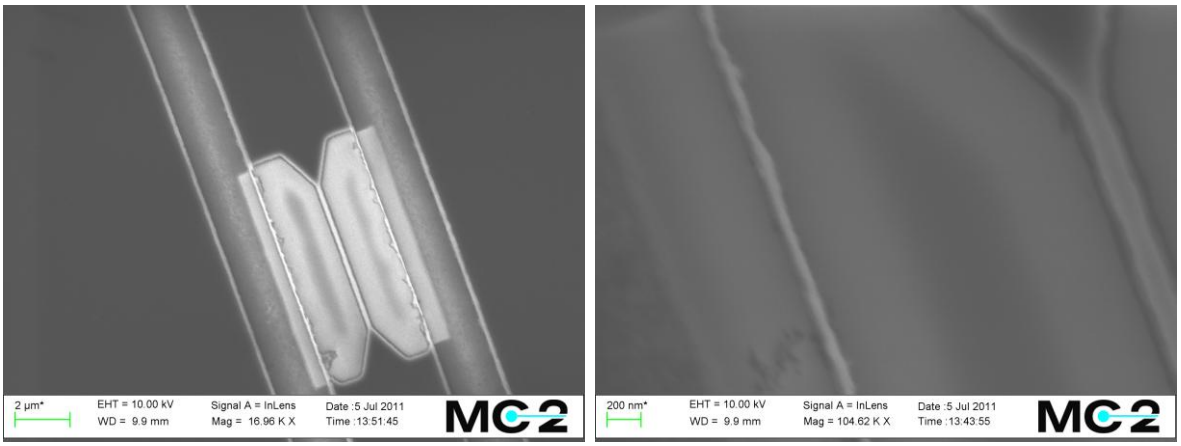

Figure 4.3 (a) SEM image of constriction in the center of resonator. (b) Zoom in SEM image of Al (or Nb) residual along the edge of central conductor.

5

Measurements

For microwave measurements, connections between feedlines on the chip and microwave signals from outside are to be designed. PCB and sample box have been designed, and dip-stick has been designed and assembled. Then the microwave properties of resonators without constrictions were pre-characterised at around 2 K in Maglab cryostat. Resonators with constrictions were measured at around 2 K and 15 mK. Related measurement steps and cryostats will be discussed in this chapter.

5.1 Design of PCB, sample box, dip-stick

5.1.1 PCB

PCBs were ordered from Hughes Circuits, Inc. The design of PCB is shown in figure 5.1, in microns. Hatched area indicates metal. The board thickness is 0.635 mm, with 17 micron copper clad on both sides. To have good bonding contacts, soft gold is deposited on top of copper layer. Through plated vias with less than 0.3 mm in diameter (not filled) are distributed over the ground plane in order to suppress unwanted ground plane resonances.

The four TLs on the PCB are connected to feedlines on the chip by bonding. On the other side U.FL-R-SMT (01) - Receptacles (figure 5.1) were soldered to the TLs on PCB to connect to microwave cables on dip-stick. A cavity of 10.2×10.2×0.25 was milled in the center of PCB to place chip.

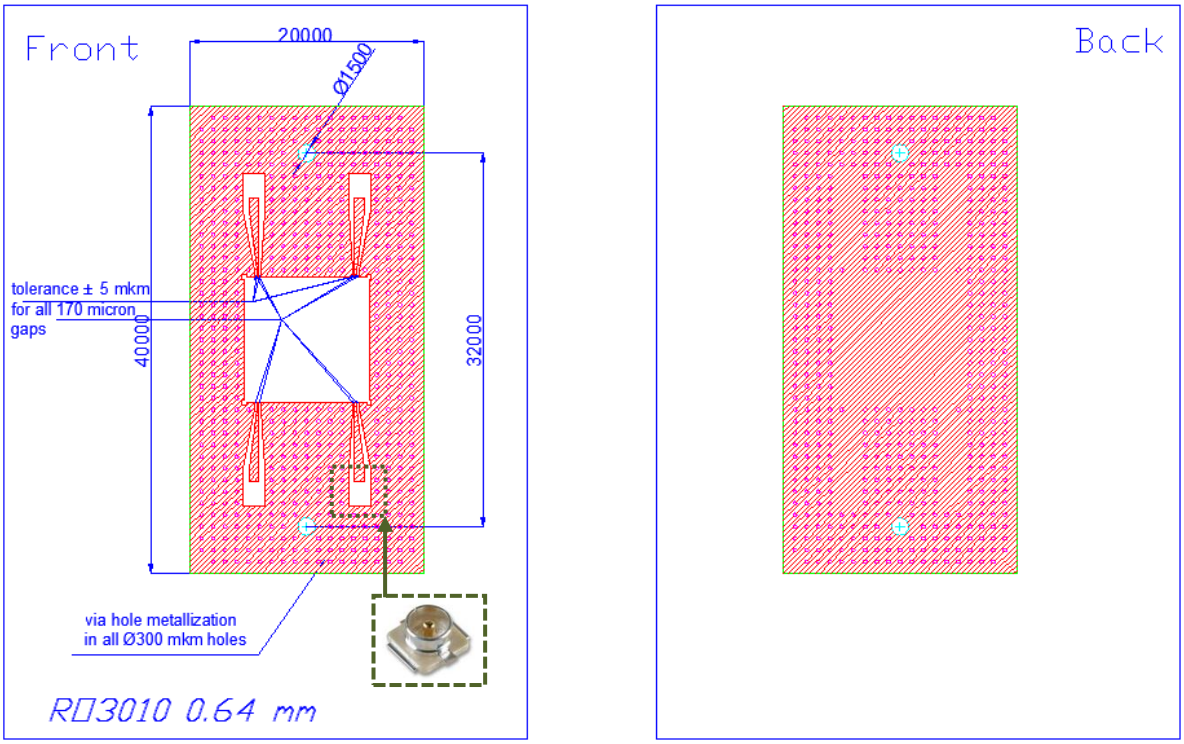

Figure 5.1 Design of PCB, in micron. The inset shows a 3D image of U.FL-R-SMT (01) - Receptacles

5.1.2 Sample box

PCB is placed in a shielded sample box which will be mounted on dipstick or other sample holders. A 3D image of sample box is shown in figure 5.2, and there are two (or four) slots to pass through microwave cables.

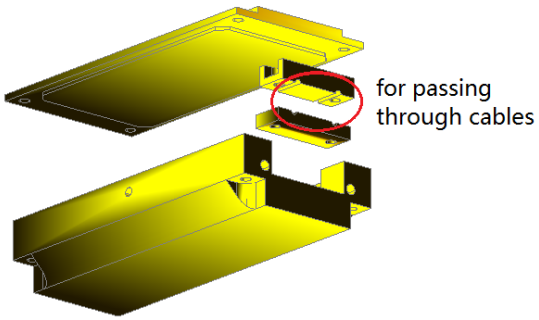

Figure 5.2 3D design of sample box

5.1.3 Dip-stick

Dip-stick is a stick which connects sample at cryogenic temperature to room temperature measurement equipment, and it is used in Maglab (which will be discussed in 5.2.1 section) in this project. Microwave cables, wires for heater, thermometer and DC signals, directional coupler and attenuators are assembled on the stick. Sample box is attached at the end of stick and surrounded by superconducting shield to screen external magnetic field of random orientations, such as the frozen field in Maglab magnet. There are some metal plates distributed along the stick to effectively cool down the cables by exchanging heat with helium gas. The sketch of dip-stick is shown in figure 5.3.

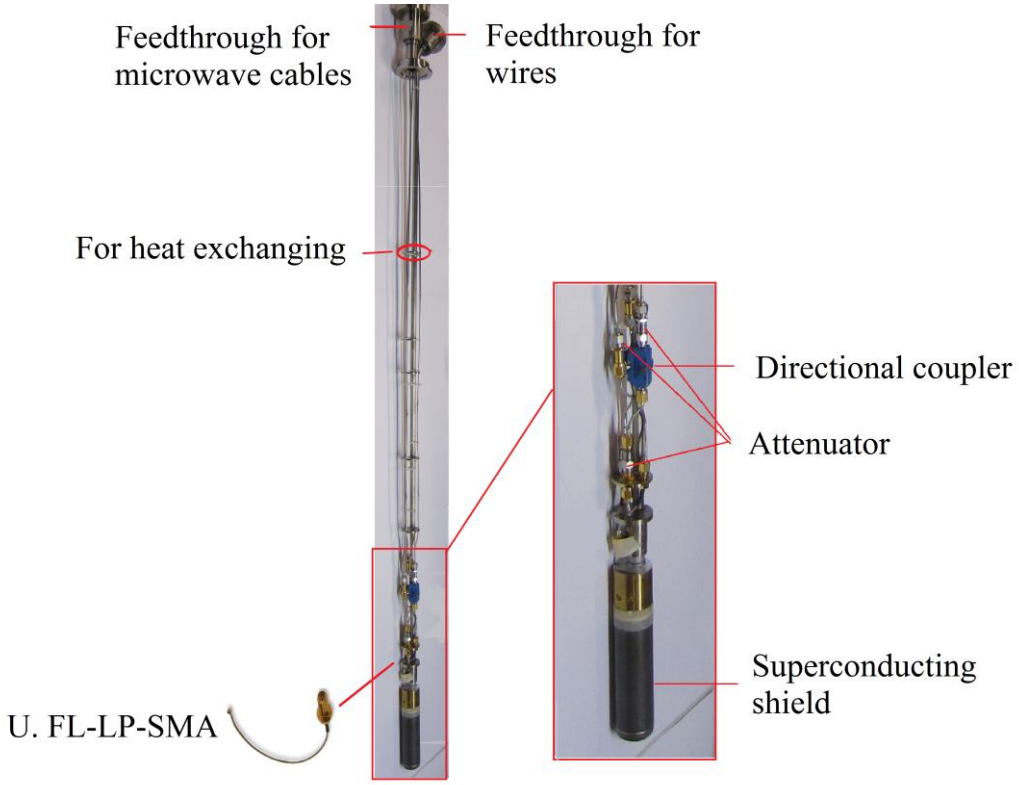

Figure 5.3 Photo of Dip-stick for Maglab measurement. Sample box is attached to dip-stick with U.FL-LP – SMA.

5.2 Measurement set-up

Microwave measurements were done below transition temperature (Tc) of Nb, which is around 8~9 K. Two cryostats were used, Maglab with base temperature of ~1.5 K and

cryofree dilution refrigerator with base temperature of ~10 mK. S parameters of the chip were measured with PNA series network analyser (figure 5.4) which covers frequency from 10 MHz to 50 GHz.

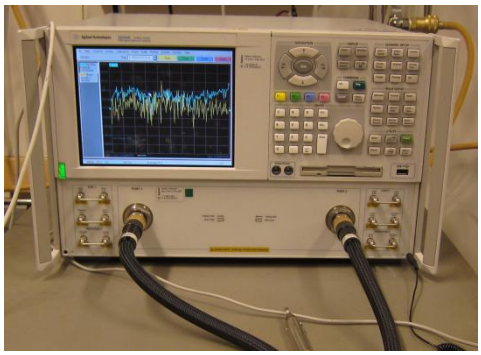

Figure 5.4 Photo of PNA series network analyser.

5.2.1 Maglab cryostat

Magnet in this cryostat can create magnetic field up to 5 T which is not needed in this project. When the magnet power supply is off, there is still frozen magnetic field with random orientations. To screen this random magnetic field, superconducting shield is placed around the sample box.

The schematics of this cryostat is shown in figure 5.5. It has 5 chambers, the inner chamber where the dip-stick sits, LHe layer, vacuum layer which is for thermal isolation, LN2 layer and one more vacuum layer around LN2 chamber. The needle valve at the bottom of the inner chamber controls LH2 level inside inner chamber. If there is LHe inside inner chamber and needle valve is closed, by pumping of the inner chamber continues, the temperature can be reduced to 1.5K.

The advantage of this cryostat is fast turn-around measurement time because the chambers are filled with LHe and LN2 all the time. However, because the helium gas is not very stable, the temperature is more difficult to control.

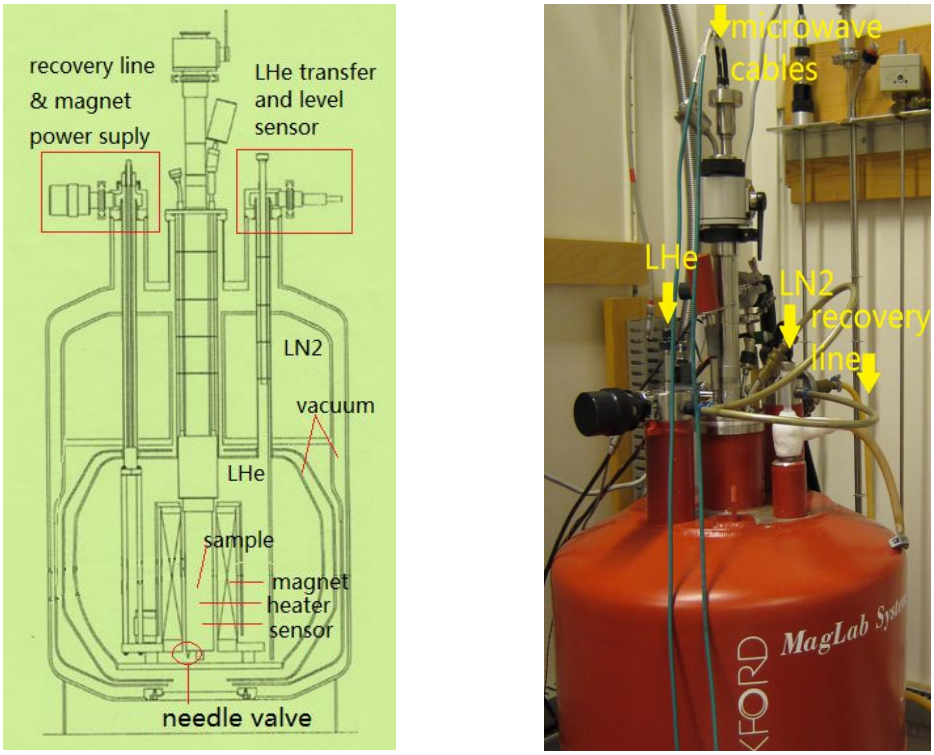

(a) (b)

Figure 5.5 (a) 2D schematics of Maglab cryostat; (b) Photo of Maglab cryostat

5.2.2 Cryofree dilution refrigerator

This set-up uses pulse tube refrigerator to cool down to ~4 K, and uses dilution refrigerator to cool down to ~10 mK.

Figure 5.6(a) gives the wiring system used during this project. The signal from the source follows line 1 and passes through four attenuators at different temperature plates, which are used to reduce the thermal noise of the signal. Additionally, the cable itself gives about 10dB attenuation.

Transmitted signal is measured via line 4. After signal passes through feedline on the chip, it goes through two circulators, high pass filter and amplifier, and it goes to the input port of network analyser. Circulators pass through the signal from the sample, but the noise from outside is absorbed by 50 Ω terminators.

The centrepiece of a dilution refrigerator is shown in figure 5.6(b). It essentially consists of the mixing chamber, the still and a counter flow heat exchanger. The circulation of ^{3}He is maintained by pumping the still. To clean ^{3}He which is evaporated in the still, it goes through nitrogen trap and helium trap. Then a flow impedance is used to condense ^{3}He. Furthermore, ^{3}He is led into the counterflow heat exchanger that consists of a continuous heat exchanger and step heat exchanger. After the heat exchanger, ^{3}He enters the mixing chamber. The return line to the still starts in the mixing chamber below the phase boundary in the ^{4}He-rich phase. On the way back to still, cold ^{3}He again flows through heat exchanger, and at the same time precool the incoming ^{3}He. During this circulation, ^{3}He atoms evaporate into ^{4}He crossing the phase boundary in the mixing chamber which leads to cooling.

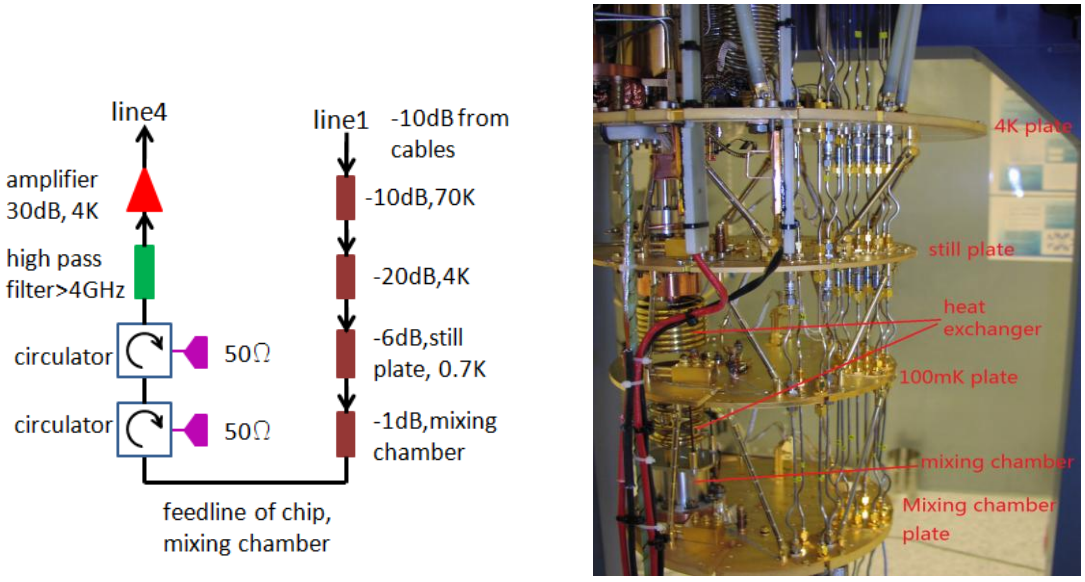

(a) (b)

Figure 5.6 (a) Schematics of the microwave wiring used during measurement; (b) Photograph identifying main items inside cryostat

6

Results

In this chapter, some of experimental results are presented. Before measurements in cryofree dilution refrigerator which takes at least one week to finish one measurement circle, it is always useful to characterise devices in Maglab first which is more effective and will give a general idea of the transmission spectra. The results in this chapter cover mainly three parts: pre-measurements of resonators without constrictions and with constrictions at around 2 K, and millikelvin measurements of resonators with constrictions.

6.1 S parameters of resonators without constrictions (~ 2 K)

6.1.1 Free ports of feedline are terminated with 50Ω

There are four ports on the chip, while two are enough for measurements. The other two free ports could be either connected with 50 Ω or grounded. Measurements were done with the following wiring system (figure 6.1).

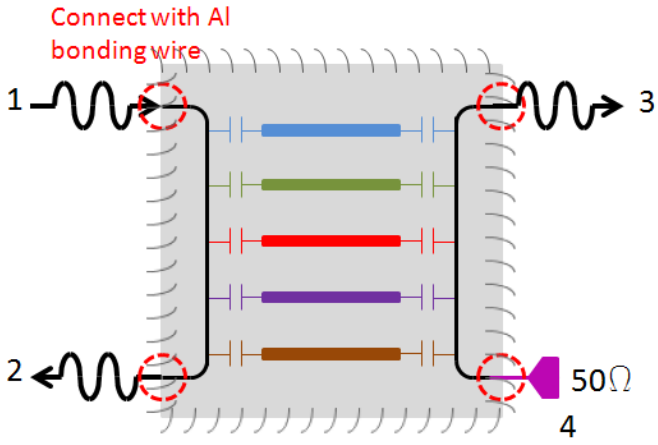

Figure 6.1 Wiring schematics of the chip

Feedline on the chip is connected to TL on PCB with Al bonding wires, and the chip is grounded with Al bonding wire at four sides. S21, S31 were measured. Since S21 and S31 are quite similar, only S21 will be discussed in this thesis.

Figure 6.2 shows the temperature dependence of the five resonances. Compare with simulations, the five peaks shift to lower frequency together, but there are still around 0.1 GHz difference between each other. The simulation and design are verified conceptually in this measurement. Because the chip is immersed in the LHe, when T increases, the peaks shift to higher frequencies above superfluid transition temperature of LHe. When T increases, the depths of peaks decrease and the peaks totally disappear after Tc of Nb.

However, there are extra peaks besides the five peaks expected from design, and magnitude and phase of each peak (figure6.3) is not symmetric. These may come from ground plane resonances which may be solved by making bondings across feedlines. Also these extra peaks may come from reflection of cables, sample box, or floating feedline.

Also, current flows at the edges of the central line and ground plane. The central line current is equal but antiparallel to the current on the ground plane. Current on both sides of ground plane are in phase (even mode). However, when T-junctions are put at feedline, the current on the ground plane is disturbed and is not in phase with current on the other side of ground plane any more. This may be an additional reason for extra peaks and asymmetry.

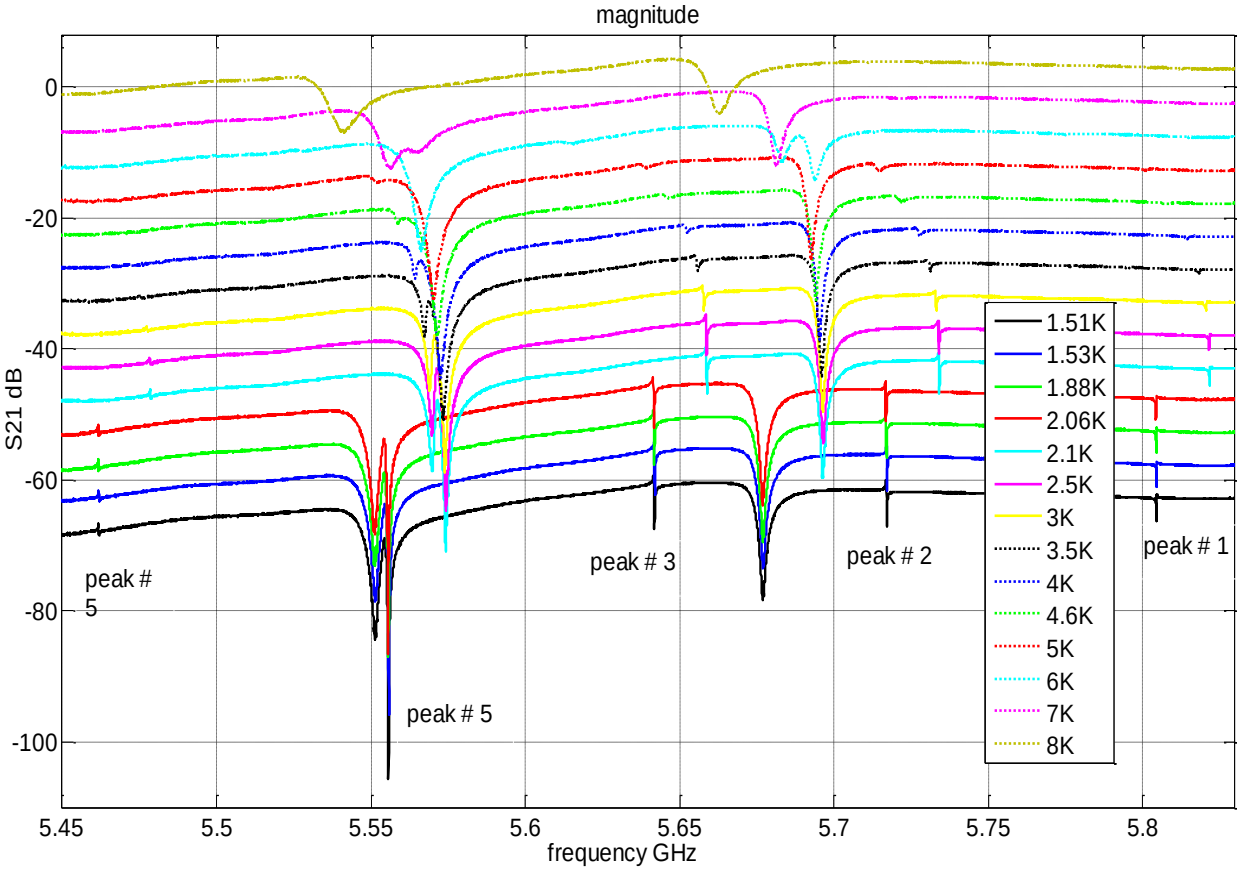

Figure 6.2 Temperature dependence the five resonances for chip without constrictions; ports 3 and 4 are terminated with 50 Ω. Each curve is offset for clarity. (Excitation Power is -38dBm)

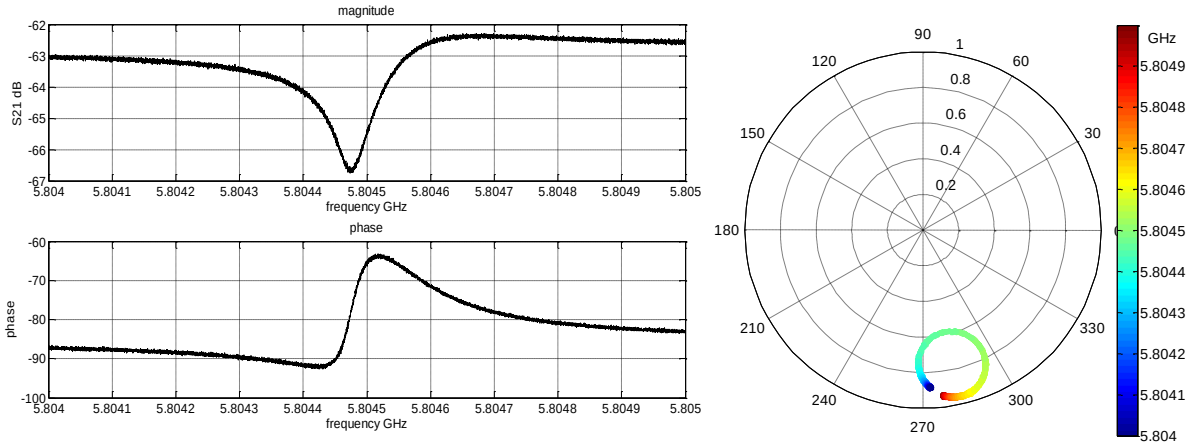

(a) (b)

Figure 6.3 (a) Zoom in picture of peak # 1; (b) Polar plot of peak # 1. (resonator without constriction, at ~1.5 K, and excitation power is -38 dBm)

Figure 6.3 shows peak # 1 in detail. The resonance depth is around 3.5dB, and magnitude and phase is asymmetric. This asymmetric line-shape may come from interference with a stray signal propagating via the ground plane. This effect may be reduced by making bondings across the feedlines. Peak # 2, # 3, # 4 and # 5 show the same asymmetric line-shape, and will not be discussed here.

Figure 6.4 gives the power dependence of peak # 1 at 1.5 K. When driving power increases, the resonance peak shifts to lower frequency and there is a bending of resonance curve. This bending comes from anharmonicity of resonance. As it will be demonstrated later, it is good to sweep frequency also from high to low values to see if there is hysteretic behaviour.

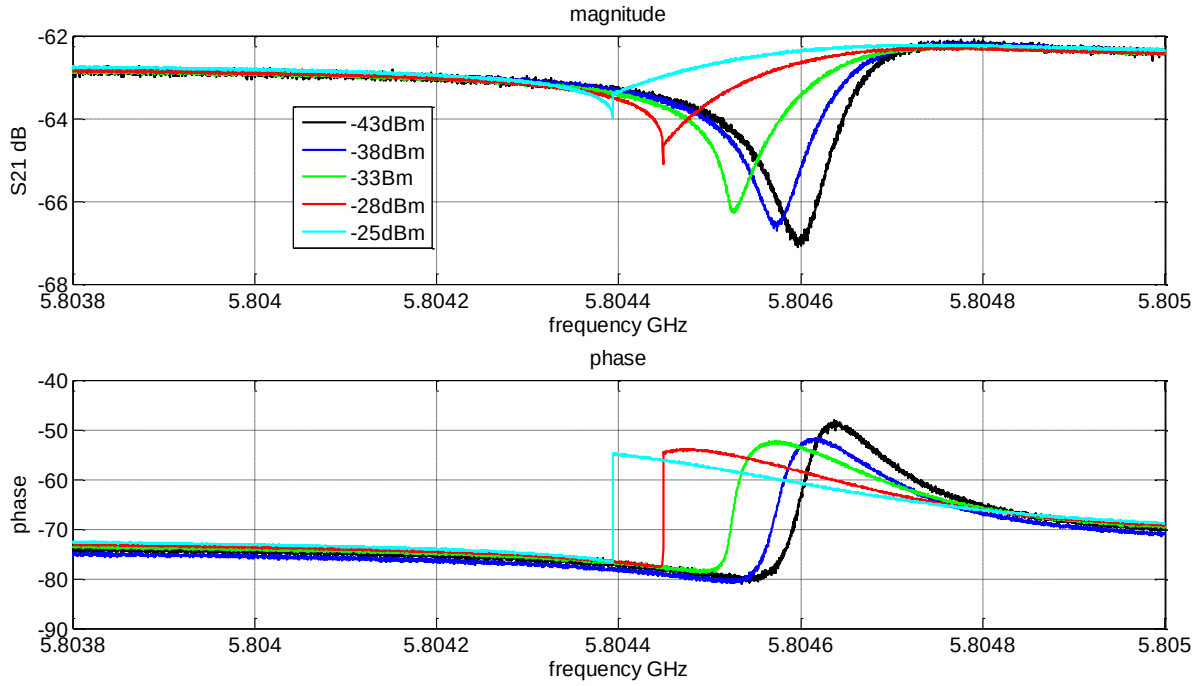

Figure 6.4 Power dependence of peak # 1 at 1.5 K (resonator without constriction).

6.1.2 Free ports of feedline are grounded

To understand the above results, further simulations (figure 6.5) were done. If the ports 3 and 4 are terminated with 50 Ω, transmission at resonance does not drop to zero. However, if ports 3 and 4 are grounded, the resonance transmission spectrum does go to 0 at resonance. It could be explained in the following way. If a resonator is coupled to two feedlines, only 50%

of radiated power goes back to excitation feedline, and it can never conceal the excitation signal.

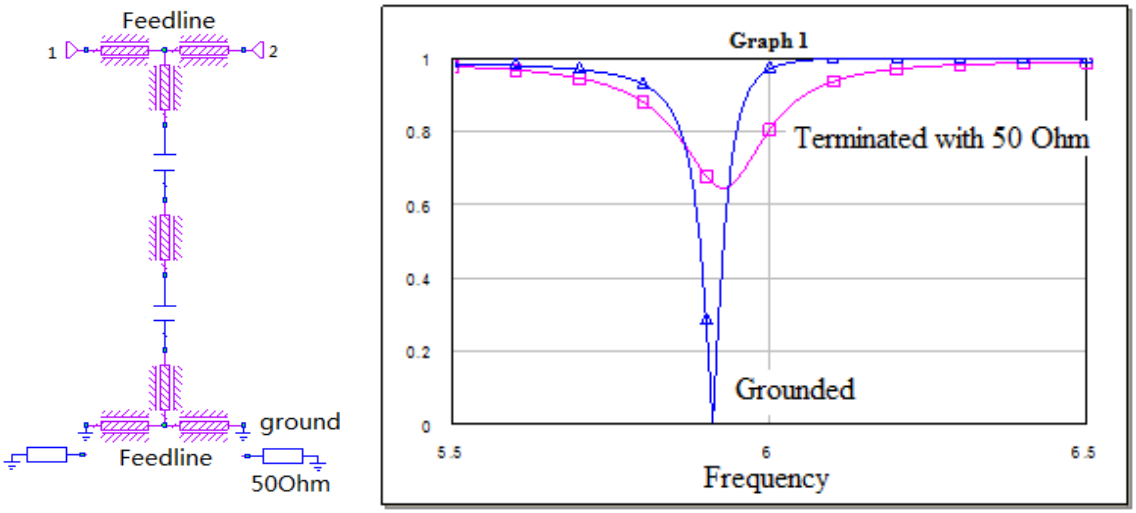

Figure 6.5 (a) Simulation model to analyze measurements; (b) simulation results

According to the simulation results, two changes were made to the chip wiring schematics to improve measurements (figure 6.6). First of all, extra bondings were made across feedlines to suppress ground plane resonances. Also free ports of feedlines were grounded to reduce energy losses at port 3 and 4.

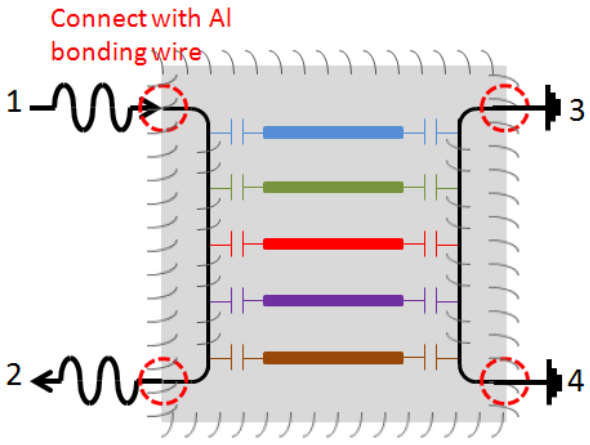

Figure 6.6 Wiring schematics of the chip after improvement.

The measurement results for the five peaks after improvement are shown in figure 6.7. The transmission spectra are indeed improved a lot. First, the background is flat in the range we

are interested in. Second, the depth of each peak increased a lot. For example, the depth of peak # 1 increases from 3.5 dB to more than 10 dB.

Figure 6.8 presents power dependence of peak # 1 at 1.6 K. When power decreases, the peak gets deeper. Qint and Qext should be calculated by fitting experimental data to circuit model. Figure 6.9 represents temperature dependence of peak # 1 when excitation power is -68 dBm. Around superfluid transition temperature, the same phenomenon happened as in figure 6.2. It is obvious from figure 6.9, although Tc of Nb is around 8 K, the resonance already disappears when temperature is above 5 K.

If the resonator is slightly anharmonic, as the resonances described above, there will be a bending of the resonance curve as the drive power is increased, and eventually results in hysteretic behaviour of the resonance curves [16]. Physical explanation of this nonlinear oscillator could be found from reference [17]. To observe this effect, 20dB attenuation on the input microwave cable is replaced into DC block. In this way, high driving power could be reached. Frequency is swept through resonance and back again, tracing out the resonance curve for different drive powers. The result is shown in figure 6.10. A bending of the resonance curve toward lower frequency as the drive power is increased is observed, and hysteretic behaviour shows up as the power increases again.

Zoom in figures of five peaks are shown in figure 6.11.

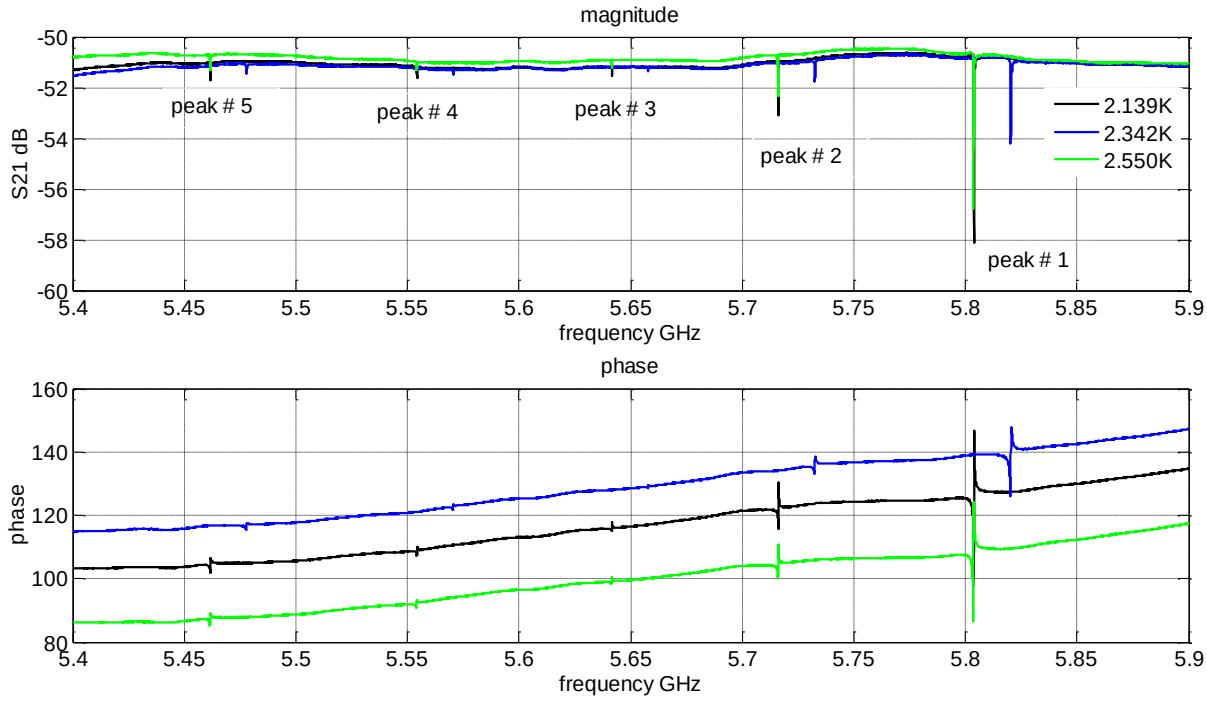

Figure 6.7 Transmission measurements of five resonators without constrictions after improvement (power sent in is -38dBm).

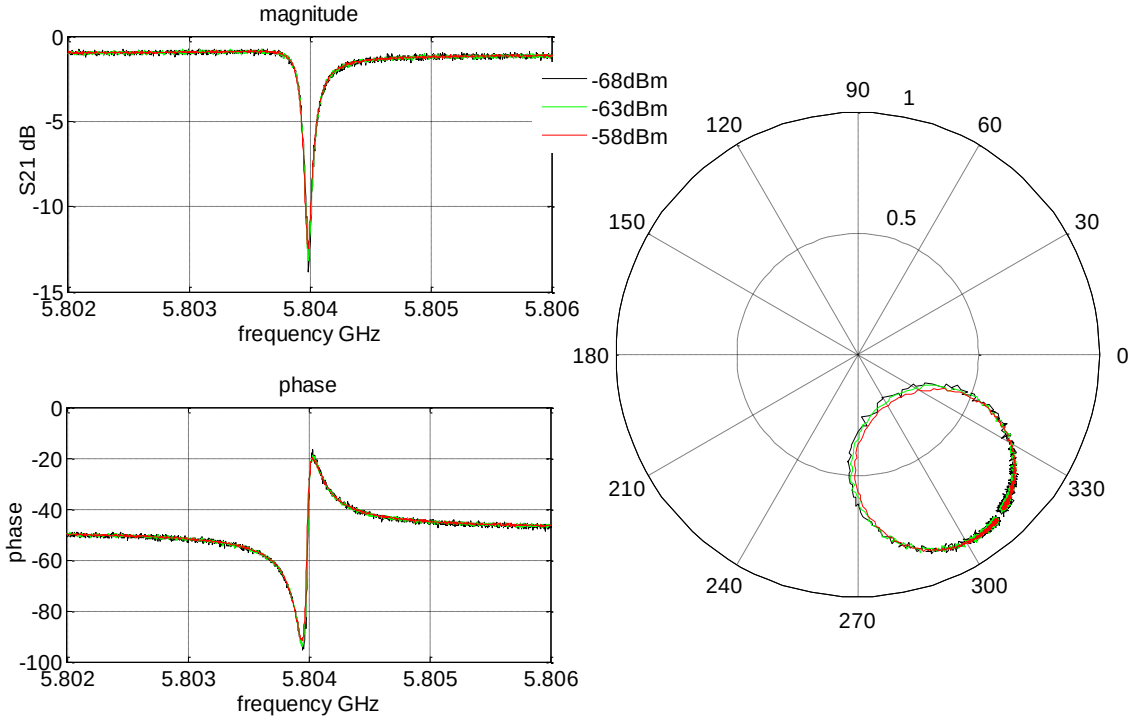

Figure 6.8 Power dependence of peak # 1at about 1.6 K (resonator without constriction, port 3 and 4 are grounded)

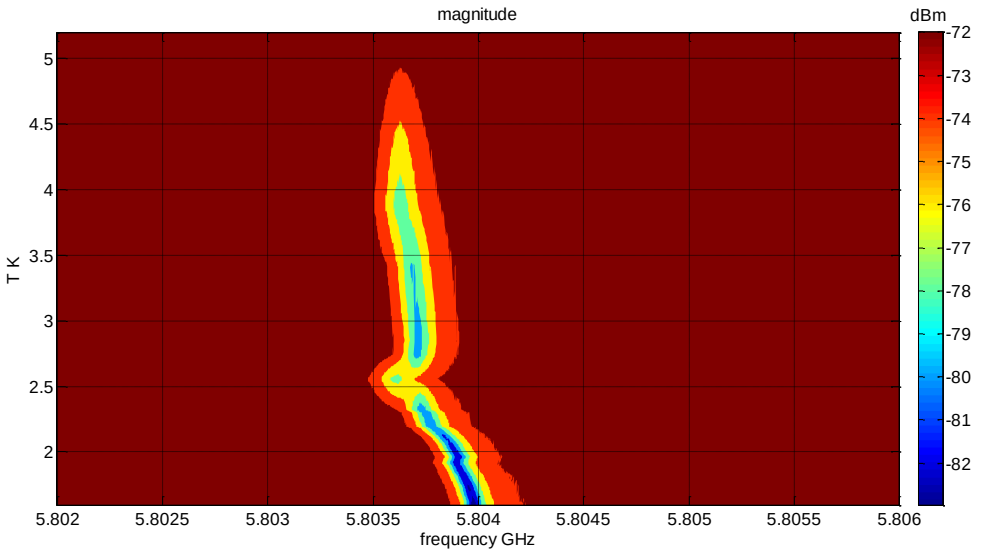

Figure 6.9 Temperature dependence of peak # 1 (resonator without constriction with ports 3 and 4 grounded, excitation power is -63dBm)

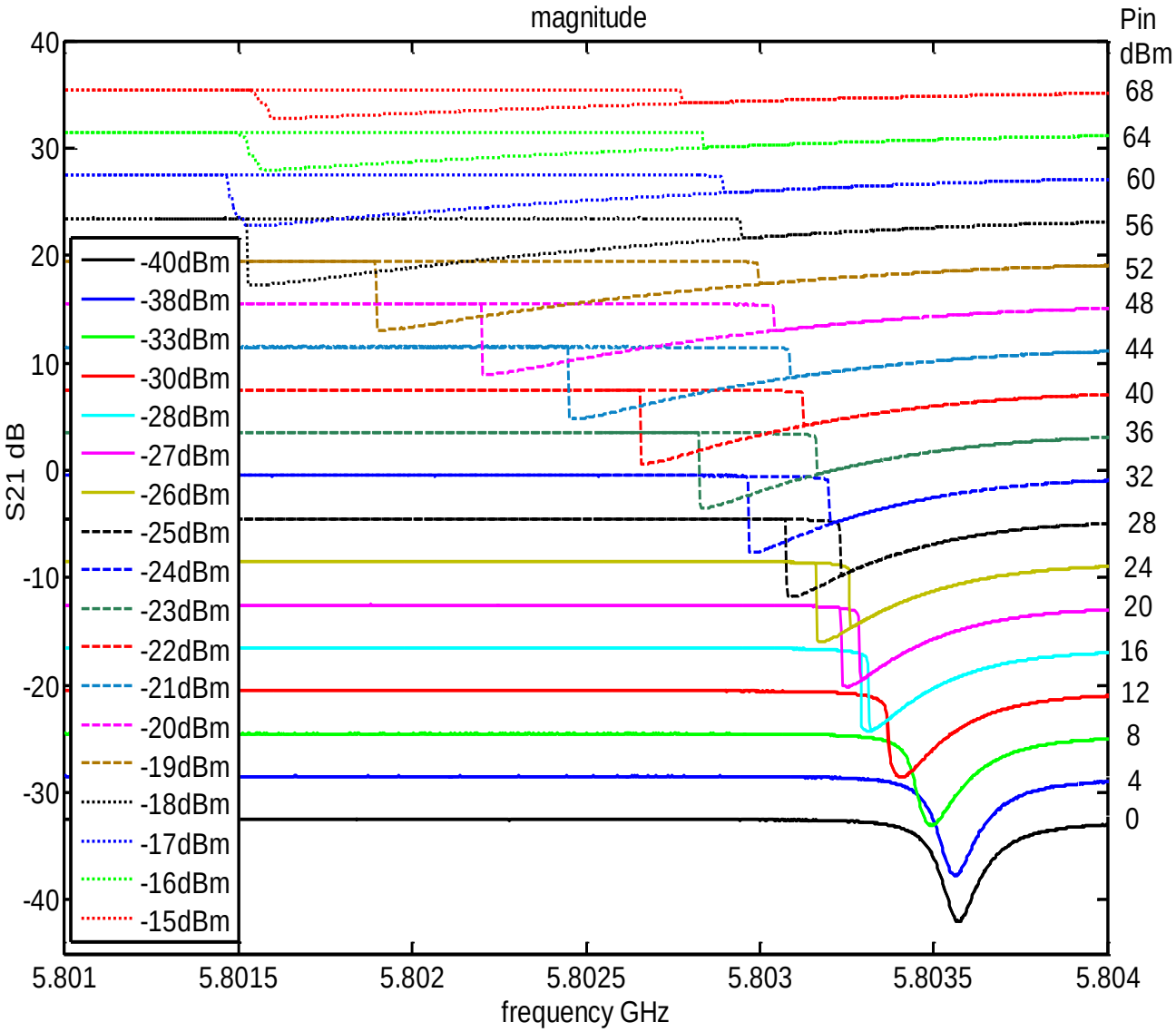

Figure 6.10 Hysteretic behaviour of peak # 1 at high driving power at ~1.9K. (Resonator without constriction) From bottom to top the driving power is increased as indicated. Each curve is offset for clarity, and offset for each curve is written on the right axis.

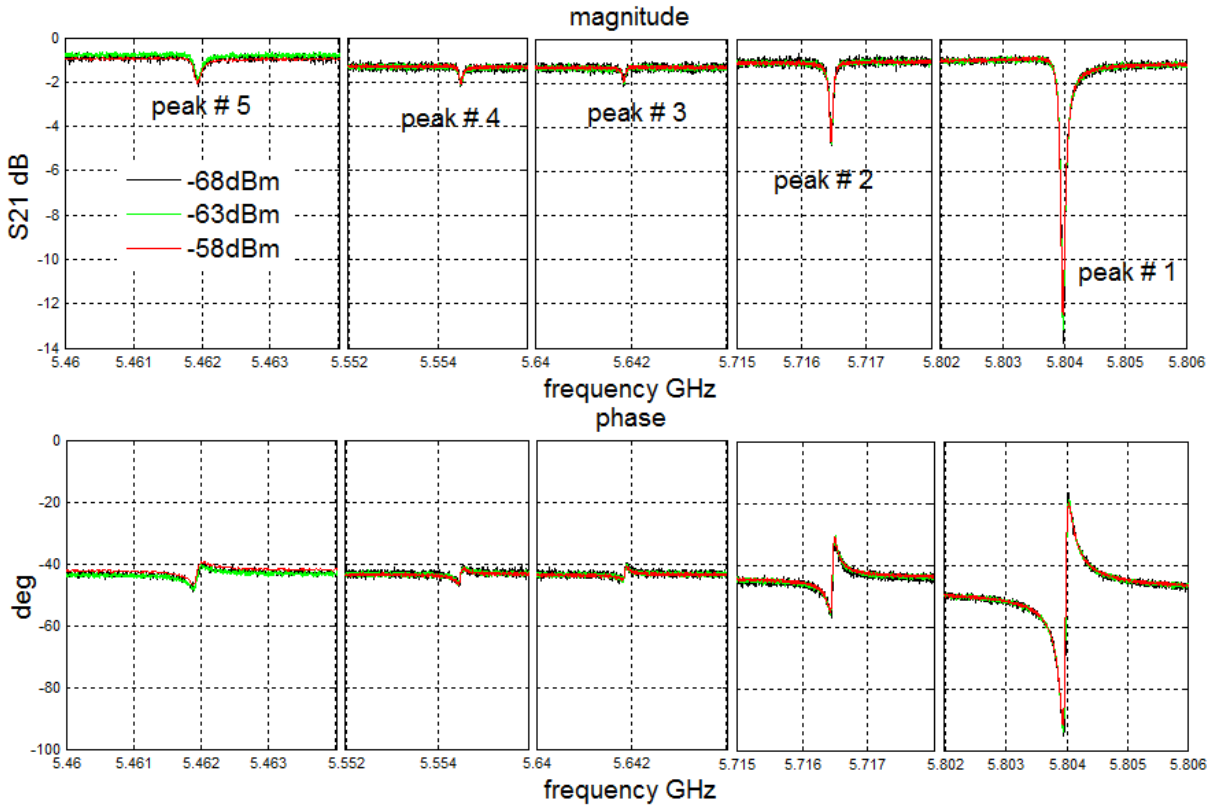

Figure 6.11 Zoom in picture for five peaks with different power at 1.6K (resonators without constrictions with ports 3 and 4 grounded)

6.2 S parameters of resonators with constrictions (~ 2 K)

Before measurements in dilution refrigerator, resonators with constrictions were pre-characterised in Maglab. Figure 6.12 shows the position of 5 peaks at 1.7 K when excitation power is -58 dBm. The data for 15 mK are presented in the next section. Figure 6.13 illustrates the temperature dependence of resonance frequency of peak # 1. It shows the same tendency as in figure 6.9, but the superfluid transition effect is not obvious in this measurement. The influence of superfluid transition to resonance frequency is determined by the LHe level in the chamber. If LHe is above sample, resonance frequency will change a lot around superfluid transition temperature of LHe. Compare with figure 6.11, 5 peaks shift to higher frequency. Probably, the shift is because of constrictions, or because the two chips are different.

Transmission spectra of resonators with constrictions were also measured (figure 6.14) at high driving power by replacing the 20dB attenuation on the dip-stick with DC block. This

high power measurement could not be done in dilution refrigerator because the strong signal saturates the cryogenic pre-amplifier.

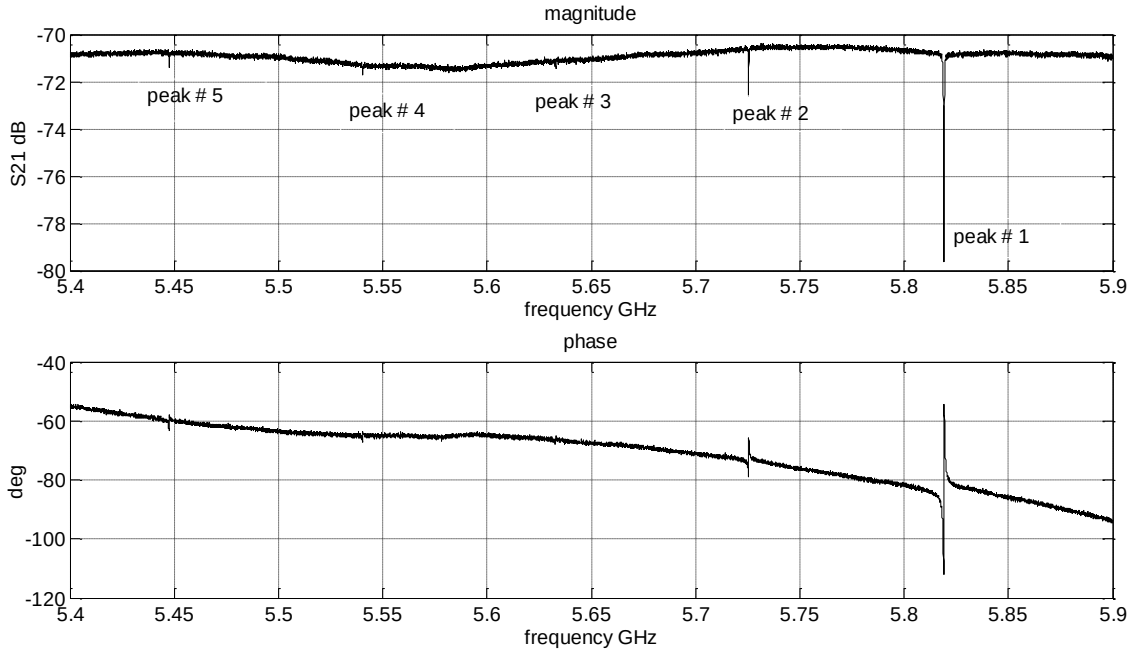

Figure 6.12 Transmission spectrum of five resonators with constrictions at 1.7 K with excitation power of -58 dBm

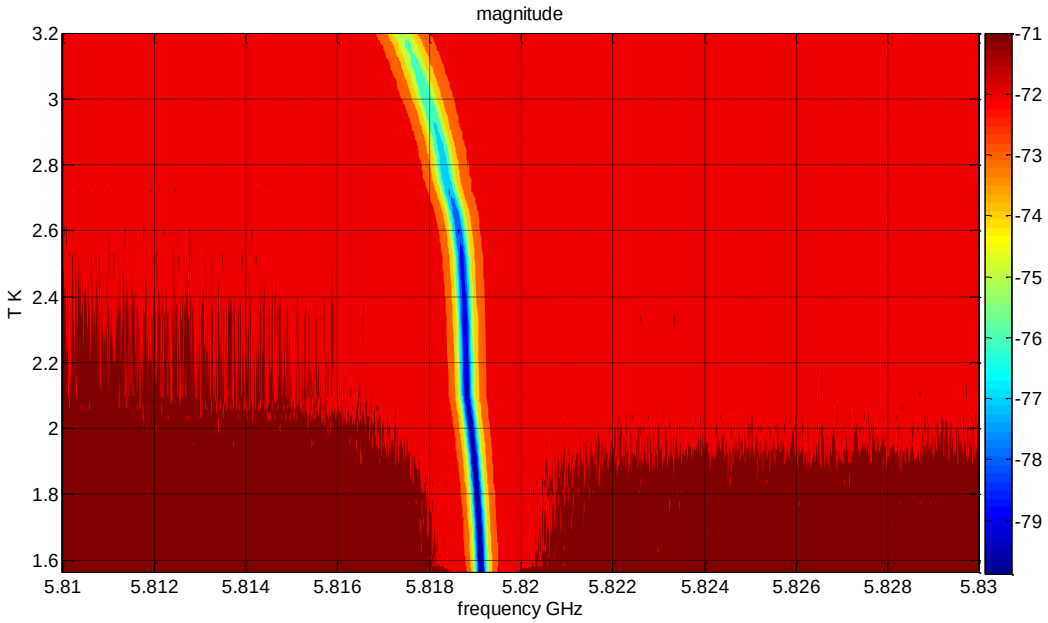

Figure 6.13 Temperature dependence of peak 1 with excitation power of -53dBm

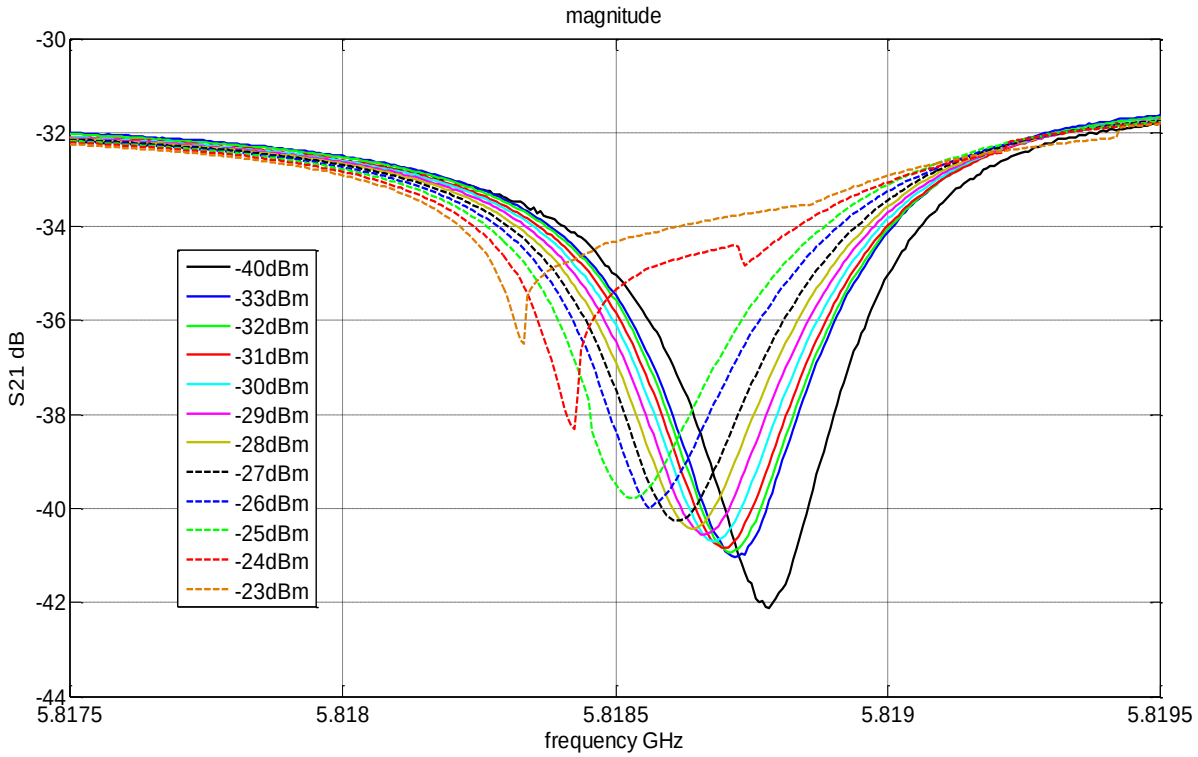

Figure 6.14 High driving power measurements of peak # 1 of resonator with constriction at 1.5 K

6.3 S parameters of resonators with constrictions (~ 15 mK)

Transmission properties of resonators with constrictions were also measured in cryofree dilution refrigerator at around 15 mK (figure 6.15). Compared to measurement at 1.7 K, the peaks are shifted to higher frequency because of reduction of kinetic inductance at low temperatures.

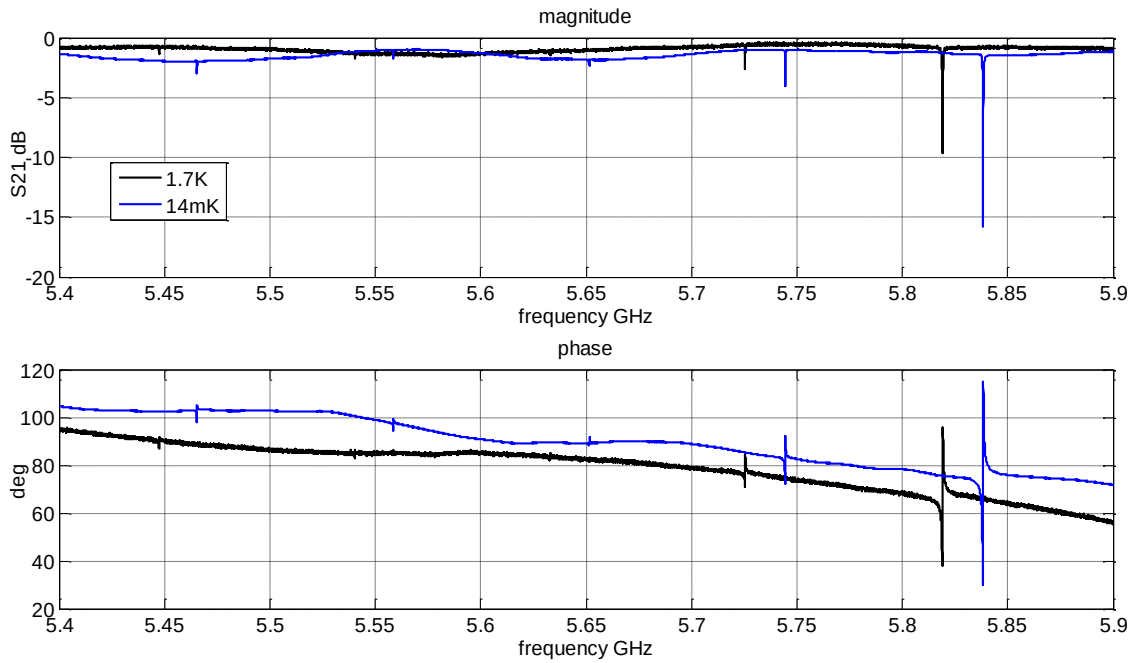

Figure 6.15 Transmission spectrum of five resonators with constrictions at 14 mK (excitation power -72 dBm) and 1.7 K (excitation power is -58 dBm)

6.3.1 Power dependence

As shown in figure 6.16, resonance shifts to lower frequency as power increases, the peak getting shallower. The same phenomenon happened to peak # 3 and peak # 4. Hysteretic behaviour of peak # 2 and peak # 5 at high driving power will be discussed in section 6.3.3.

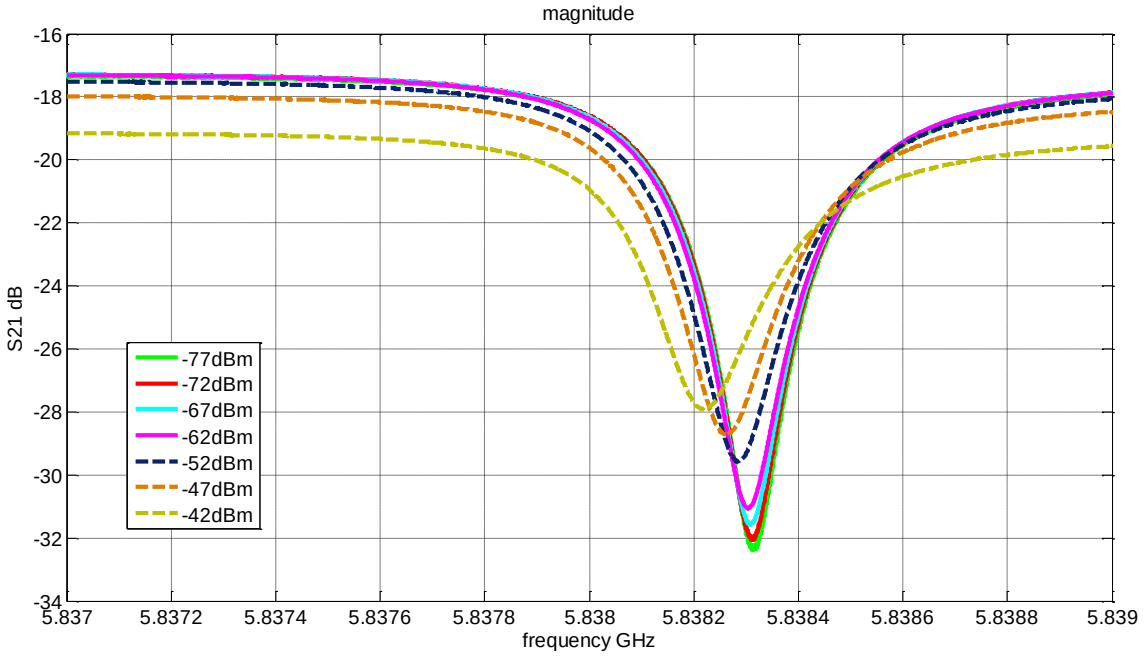

Figure 6.16 Power dependence of peak # 1 of resonator with constriction at 14 mK.

6.3.2 Temperature dependence

Figure 6.17 illustrates temperature dependence of resonance of peak # 1 with excitation power sent in of -82 dBm, and the tendency is the same as for the other peaks at this power level. When temperature decreases, the resonance frequency shifts to higher value due to the decrease of kinetic inductance, because $L_K = \frac{4\pi\lambda^2}{d}$, then the resonance frequency saturates at 5.83833GHz, since kinetic inductance is almost constant when temperature approaches zero.

When power increases, resonance curves start to show nonlinearity, and this effect was observed for peak # 2 and peak # 5 at the highest power level available in the dilution refrigerator. The temperature dependence of the nonlinear curve is shown in figure 6.18.

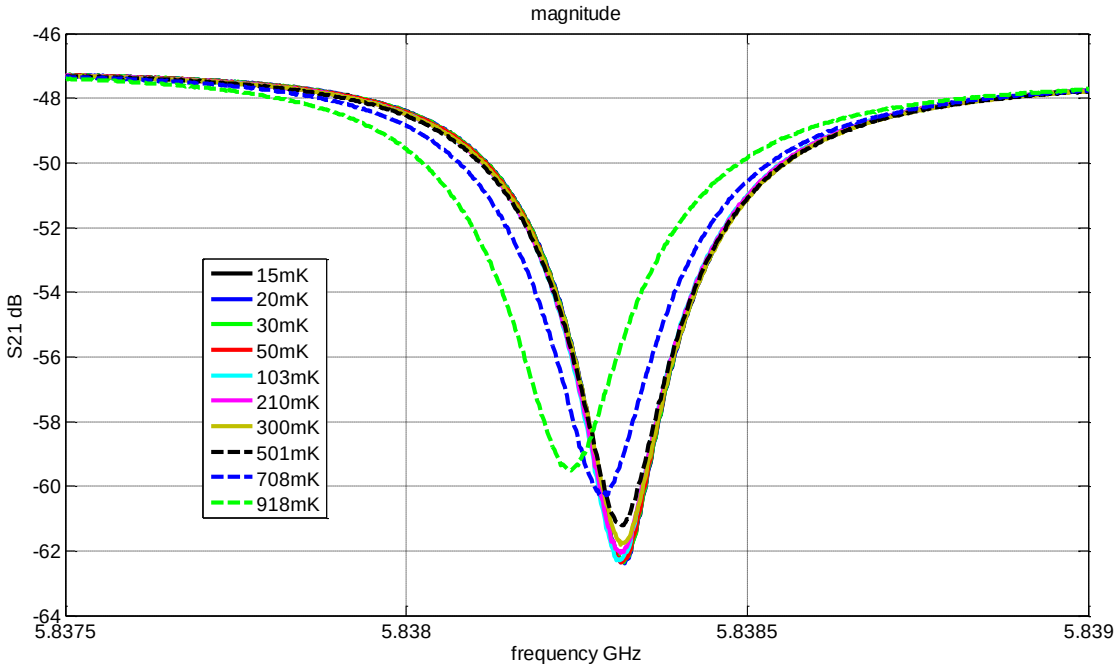

Figure 6.17 Temperature dependence of peak # 1of resonator with constriction with excitation power of -82 dBm

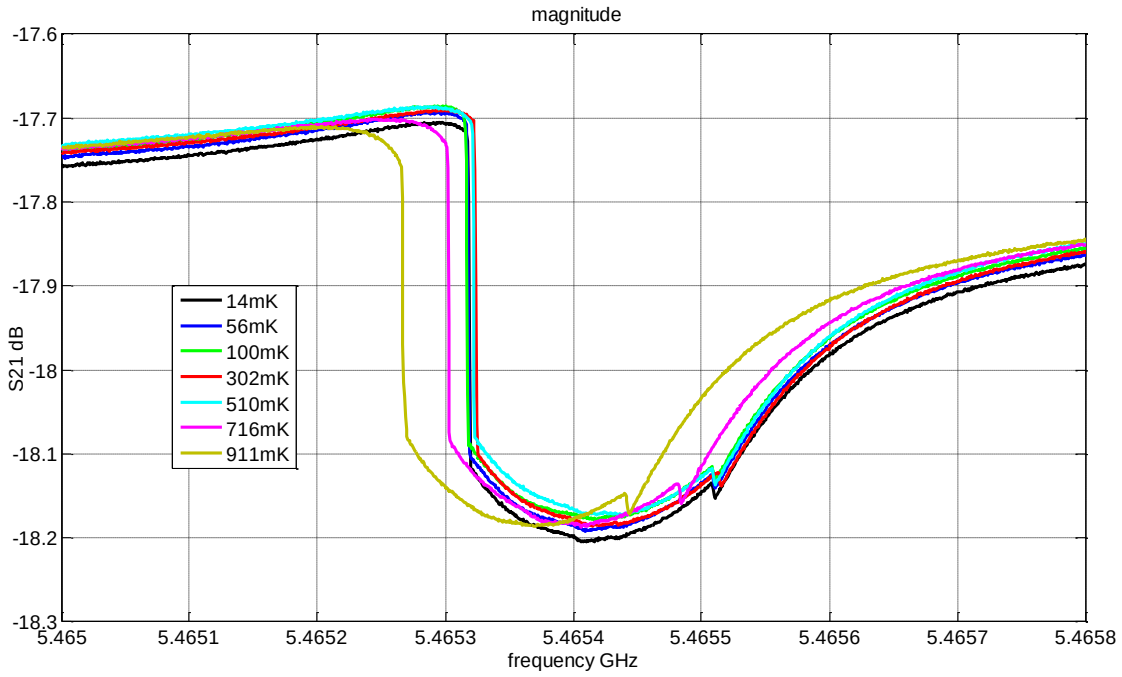

Figure 6.18 Temperature dependence of the nonlinear curve of peak # 5 (resonator with constriction), with excitation power of -57 dBm

6.3.3 Hysteretic behaviour at high power

If power is increased, there is a bending of resonance curve, which eventually results in hysteretic behaviour of the resonance curve (figure 6.19, 6.20).

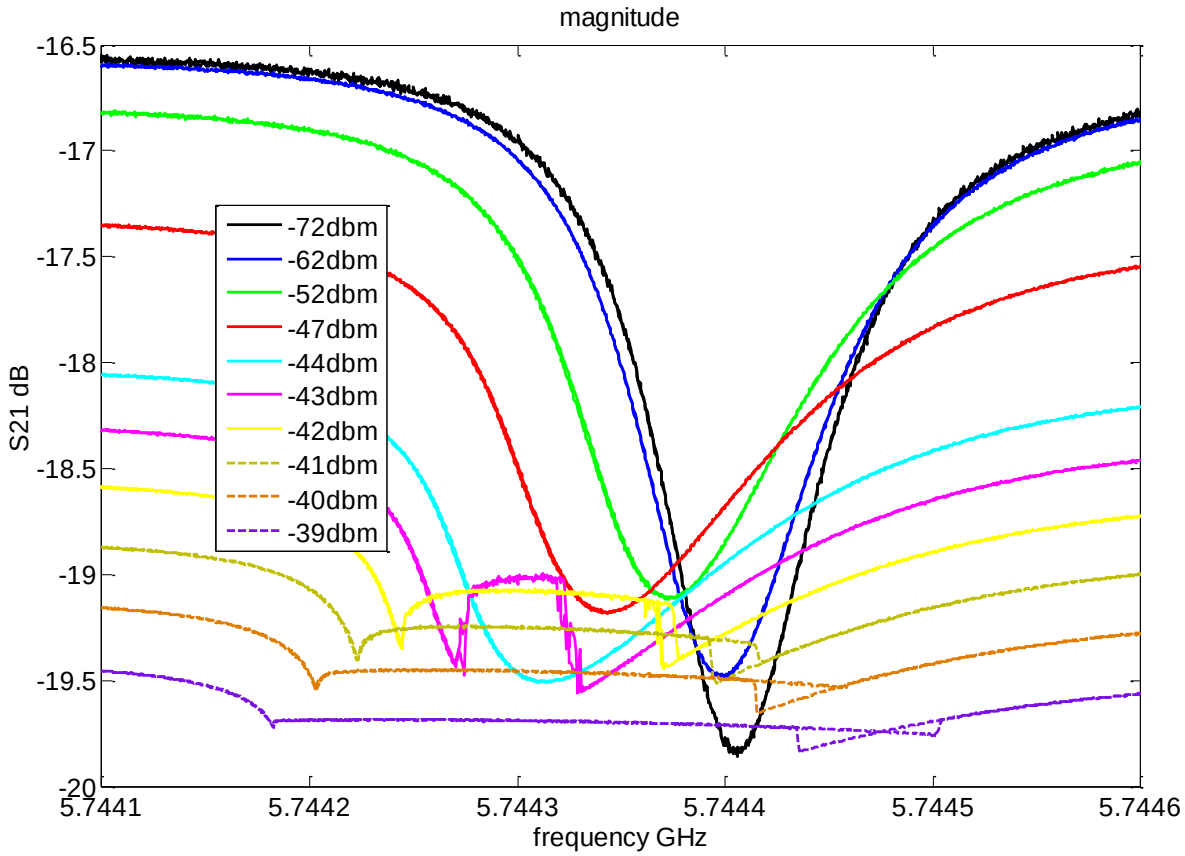

Figure 6.19 Hysteretic behaviour of peak # 2 at 11 mK

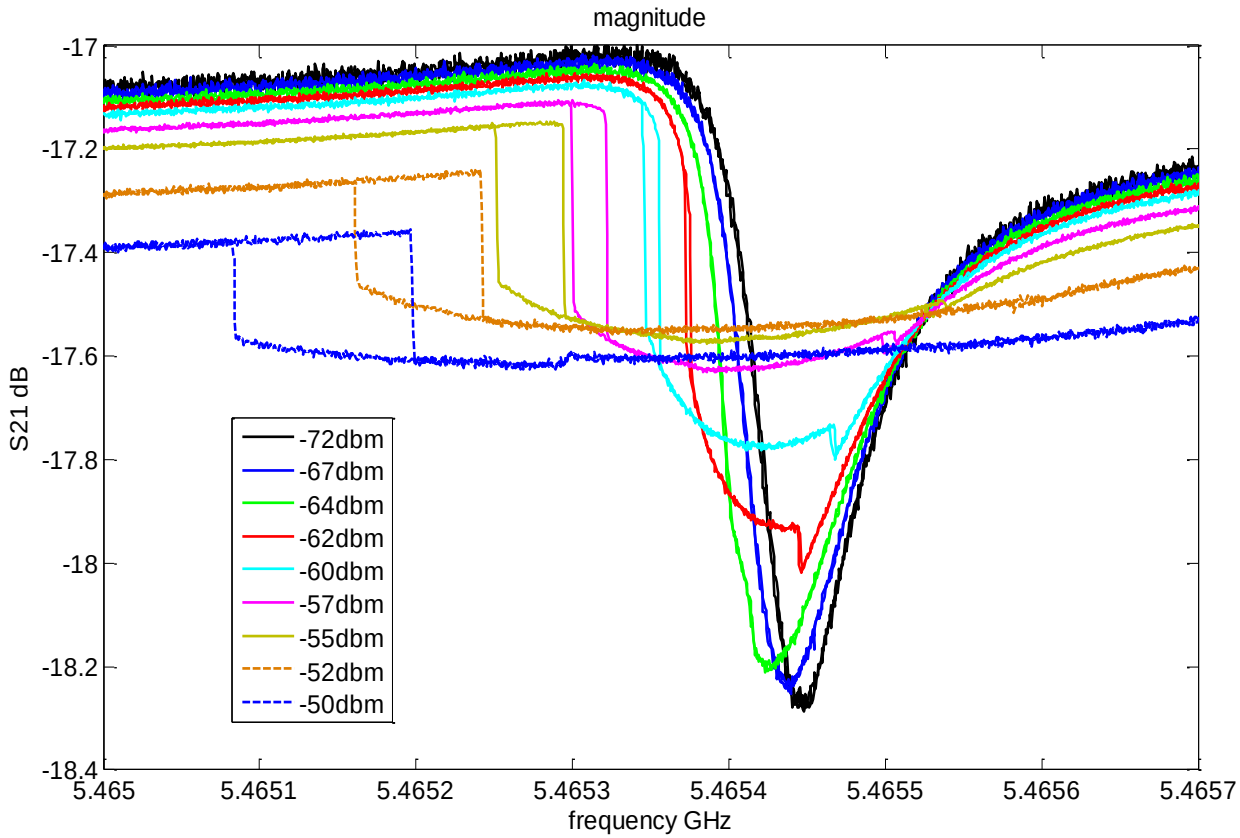

Figure 6.20 Hysteretic behaviour of peak # 5 at 11 mK

7

Analysis

7.1 Fitting Resonator Parameters

A TL resonator is a distributed device with voltages and currents varying in magnitude and phase over its length. Because the five resonators on the chip have different resonance frequencies, they can be considered independently. The distributed element representation of the resonator is shown below (figure 7.1). During this project, one side of the resonator is grounded via coupling capacitance Ck, and the other side is connected to feedline through which transmission spectra are measured. C_K is coupling capacitance which couples resonator with outside circuit. R_L is characteristic impedance of input (and output) microwave cables.

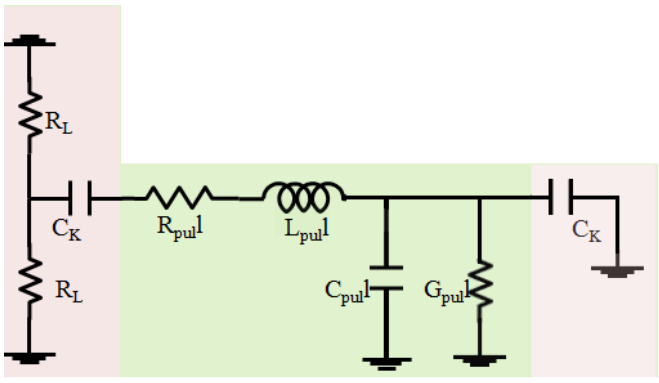

Figure 7.1 Distributed element representation of the resonator

7.1.1 Calculation of Qext and Qint

Around resonance, the properties of a TL resonator can be modelled by a parallel LCR oscillator (figure 7.2).

The series connection of C_k and R_L can be transformed into a Norton equivalent parallel connection of a resistor R^* and a capacitor C^*.

$$R^* = \frac{1}{{\omega_n}^2 {C_k}^2 \frac{R_L}{2}}$$

$$C^* = C_k$$

$$Q_{\text{int}} = \omega_n RC$$

$$Q_L = \omega_n (C + C^* + C_k)\left(\frac{1}{\frac{1}{R} + \frac{1}{R^*}}\right)$$

$$Q_{\text{ext}} = \frac{1}{\frac{1}{Q_L} - \frac{1}{Q_{\text{int}}}} = \frac{2CR(C + 2C_k)\omega_n}{C_k(-4 + CRC_k R_L \omega_n^2)}$$

The resonance frequency shifted by the capacitive loading.

$$\omega_n = \frac{1}{\sqrt{L_n (C + C^* + C_k)}} \quad (*)$$

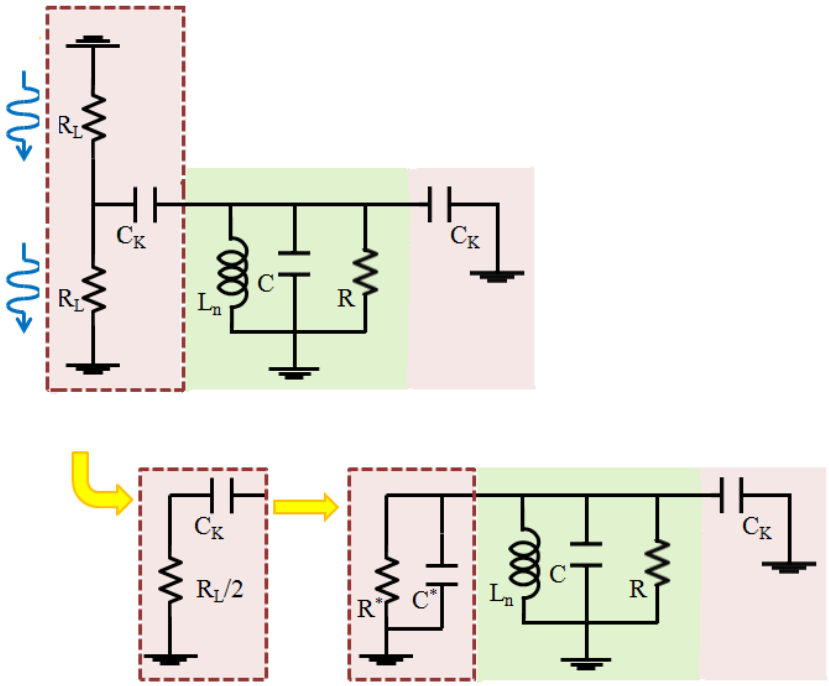

Figure 7.2 Distributed element representation of the resonator to calculate Qext and Qint

7.1.2 Calculation of S21

According to figure 7.3,

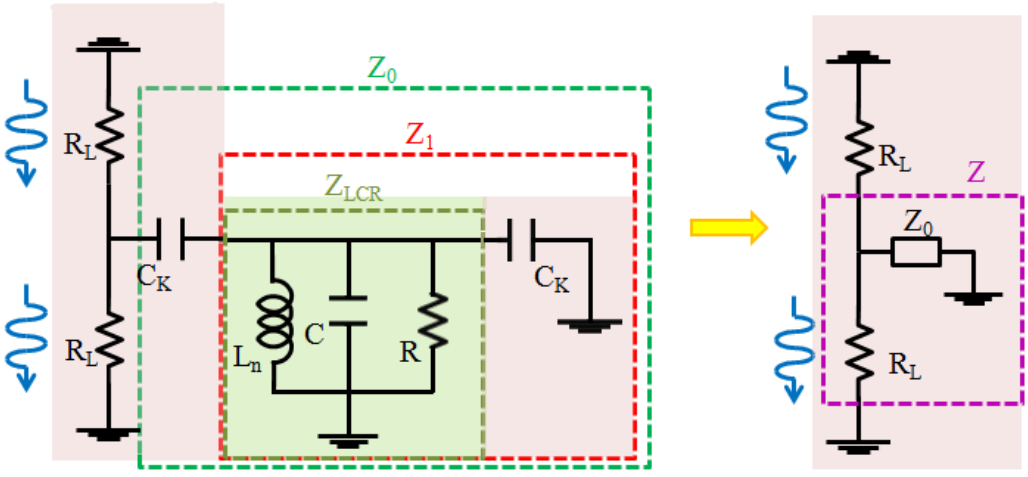

Figure 7.3 Distributed element representation of the resonator to calculate S21

$$Z_{\mathrm{LCR}} = \frac{1}{\frac{1}{i\omega L_n} + i\omega C + \frac{1}{R}}$$

$$Z_1 = \frac{1}{\frac{1}{Z_{\mathrm{LCR}}} + i\omega C_k}$$

$$Z_0 = Z_1 + \frac{1}{i\omega C_k}$$

$$Z = \frac{1}{\frac{1}{Z_0} + \frac{1}{R_L}}$$

$$S_{21} = \frac{2Z}{Z + R_L}$$

$$= \frac{-2\mathrm{L_n}\omega + 2i\mathrm{R}(1 - (\mathrm{C} + 2C_k)\mathrm{L_n}\omega^2)}{2i\mathrm{R} - (2\mathrm{L_n} + C_k R_L \mathrm{R})\omega - i\mathrm{L_n}(2\mathrm{CR} + C_k(R_L + 4\mathrm{R}))\omega^2 + C_k(\mathrm{C} + C_k)\mathrm{L_n}R_L\mathrm{R}\omega^3}$$

Replace $\mathrm{L_n}$ into ω_n, R and C into $\mathrm{Q_{int}}$ and $\mathrm{Q_{ext}}$, then S_{21} becomes

$$S_{21} = \frac{(8Q_{\mathrm{int}}\omega\omega_n + 2iQ_{\mathrm{ext}}(-4 + C_k Q_{\mathrm{int}} R_L \omega_n)(i\omega\omega_n + Q_{\mathrm{int}}(-\omega^2 + {\omega_n}^2)))}{(2Q_{\mathrm{int}}\omega(C_k R_L \omega(-Q_{\mathrm{int}}\omega + 2i\omega_n) + 4\omega_n) + Q_{\mathrm{ext}}(-2i + C_k R_L \omega)(-4 + C_k Q_{\mathrm{int}} R_L \omega_n)(-i\omega\omega_n + Q_{\mathrm{int}}(\omega - \omega_n)(\omega + \omega_n)))}$$

To prove the accuracy of calculations above, a discussion of S21 as a function of frequency has been done, and the results are shown in figure 7.4. At critical coupling, S21 is around 0.5 at resonance as expected. When Qint increases, Qtot, which controls the half width half maximum (HWHM), also increases, so the peak gets deeper. If external coupling gets stronger (Ck increases), the peak is not symmetric anymore. In the polar plot, the resonance circle rotates not only in phase, but also shifts up (for positive Ck) and down (for negative Ck). Inset figure shows the shift of resonance frequency induced by changes in Ck, which is in agreement with formula (*) in section 7.1.1.

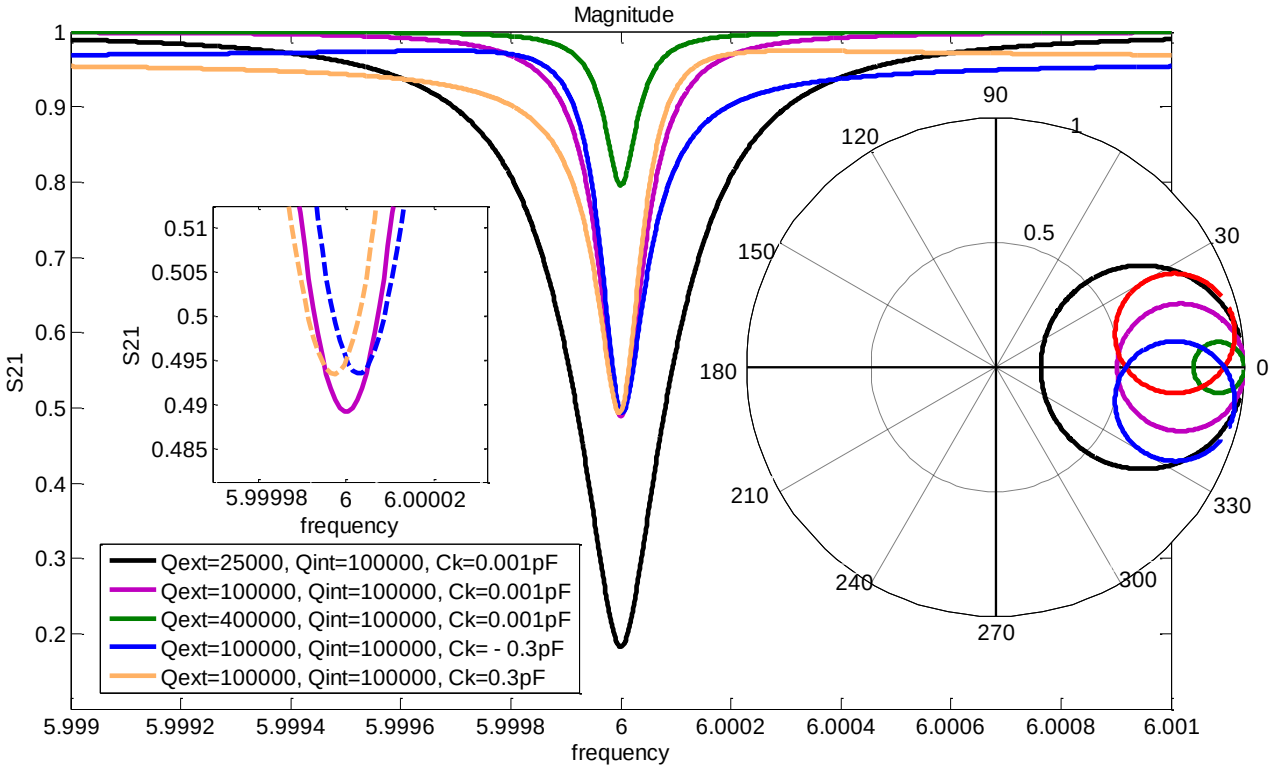

Figure 7.4 S21 versus frequency deduced from circuit model. Inset (left) shows the shift of resonance frequency induced by Ck, and inset (right) gives resonance circles.

7.1.3 Data fitting

Data fitting was done in Matlab. Figure 7.5 gives an example of data fitting for peak # 1 of resonators without constrictions at 1.6 K, and excitation power is -68 dBm. From figure 7.5, we see that the transmission data are well described by theoretical formula deduced above.

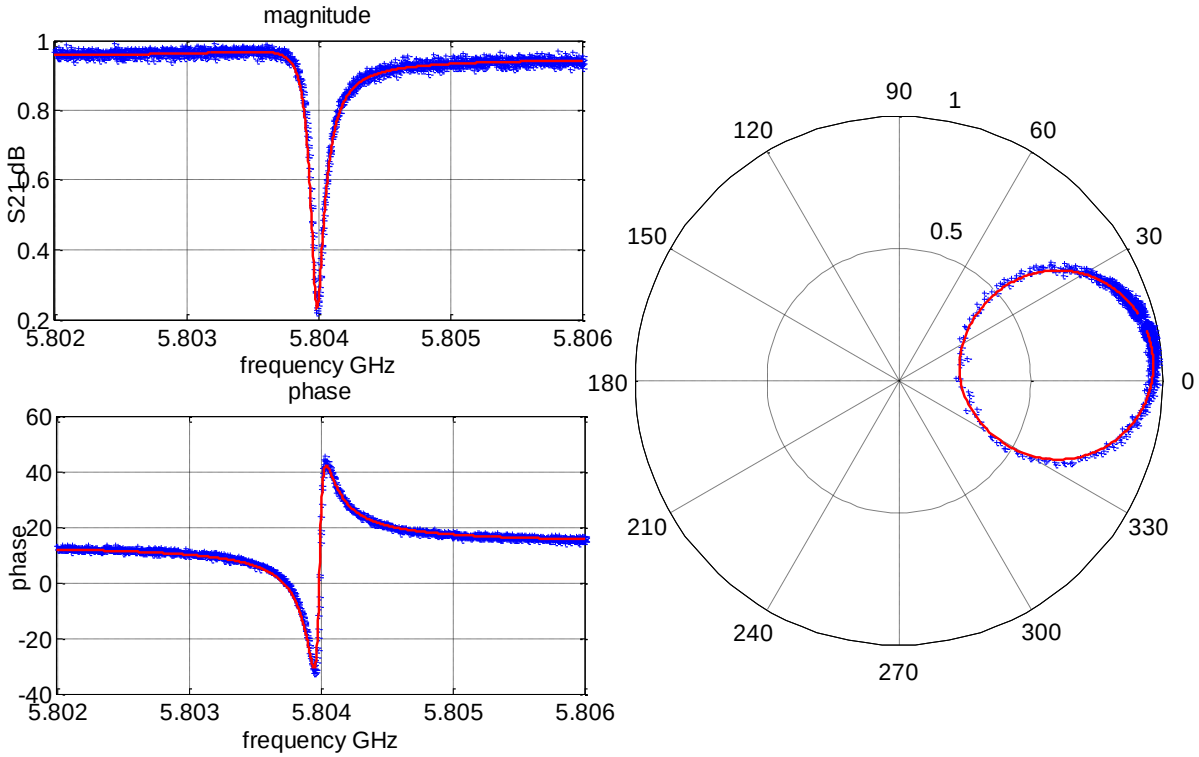

Figure 7.5 An example of data fitting. Fitting for resonators without constrictions. (1.6K, excitation power is -68 dBm) Blue crosses indicates experimental data, and red curves are for theoretical fitting.

By fitting theoretical formula to experimental curves, parameters of the resonator, such as Ck, Qext and Qint, could be extracted, and the results of resonators without constrictions, and with constrictions are listed in table 7.1, 7.2 and 7.3.

Table 7.1 Parameters of resonators without constrictions at 1.6 K (excitation pown is -82 dBm)

	Q	Qint	Qext	Ck/pF	f0/GHz
Peak1	32000	126500	42836	-0.27	5.803985
Peak2	68000	103000	200110	0.008	5.716465
Peak3	94000	103000	1075800	0.001	5.64186
Peak4	95000	103000	1223125	-0.003	5.5545
Peak5	94500	102300	1239400	0.00007	5.46195

Table 7.2 Parameters of resonators with constrictions at 1.6 K (excitation power is -77 dBm)

	Q	Qint	Qext	Ck/pF	F0/GHz
Peak1	15000	43000	23036	-0.1	5.81913
Peak2	34200	43000	167110	0.001	5.72548
Peak3	44900	46500	1304900	0.0003	5.63294
Peak4	45200	46500	1616800	0.0002	5.55335
Peak5	45500	46800	1638000	0.00008	5.4476

Table 7.3 Parameters of resonators with constrictions at 14 mK (excitation power is -72 dBm)

	Q	Qint	Qext	Ck/pF	F0/GHz
Peak1	13700	69850	17043	-0.1	5.838309
Peak2	49100	69750	165850	-0.09	5.744405
Peak3	64800	69750	913090	0.43	5.65153
Peak4	63000	70050	625980	-0.188	5.558605
Peak5	59950	70300	407200	-0.5	5.46544

From the three tables above, Qext has the tendency to increase from peak #1 to peak #5, which is consistent with design. Qint of resonators without constrictions is ~100000 at 1.6K. Constrictions introduce extra internal losses to the resonators and Qint decreases to 45000 of resonators with constrictions at 1.6K. When temperature decreases from 1.6K to 14mK, Qint increases to 70000.

High coupling capacitance gives asymmetry of magnitude and phase plots.

7.2 Kinetic inductance

The contribution of the kinetic inductance in normal conductors can only be significant at very high frequencies. However, the kinetic inductance sometimes plays an important role in superconductors. When temperature decreases, resonances shift to higher frequency due kinetic inductance. Resonance frequency as a function of temperature of peak # 1 of resonator with constriction (figure 6.15) with power of -35dBm is plotted in figure 7.4.

The fit to theoretical temperature dependence of kinetic inductance gives Tc of Nb thin film 10.67K.

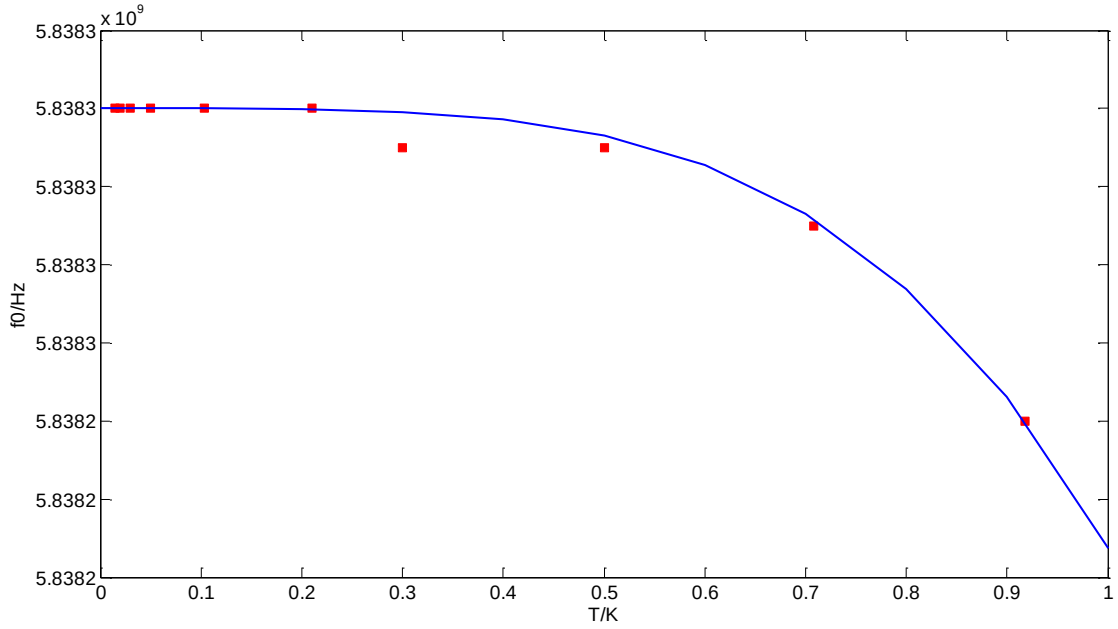

Figure 7.4 Kinetic inductance fitting to resonance frequency at different Ts. Red dots are experimental data, blue line is fitting.

$$L = Lmagnetic + Lkinetic = 2\pi\lambda + 2\pi\lambda = 4\pi\lambda$$

$$\lambda = \frac{\lambda(0)}{\sqrt{1 - (\frac{T}{Tc})^4}}$$

$$f_0 = \frac{1}{2\pi\sqrt{LC}}$$

7.3 Hysteretic behaviour

Hysteretic behaviour of transmission curves were observed when diving signal is strong enough. The frequency is swept through resonance and back again, tracing out the resonance curve for different diving powers. To have a quantitative understanding of the hysteretic behaviour, we focus on the non-linearity of peak # 2 and peak # 5 (figure 6.17 and 6.18). The positions of each subpeaks, marked with A, B, C and D, as a function of $\sqrt{P}$ is plot in figure 7.5 (C) and (D).

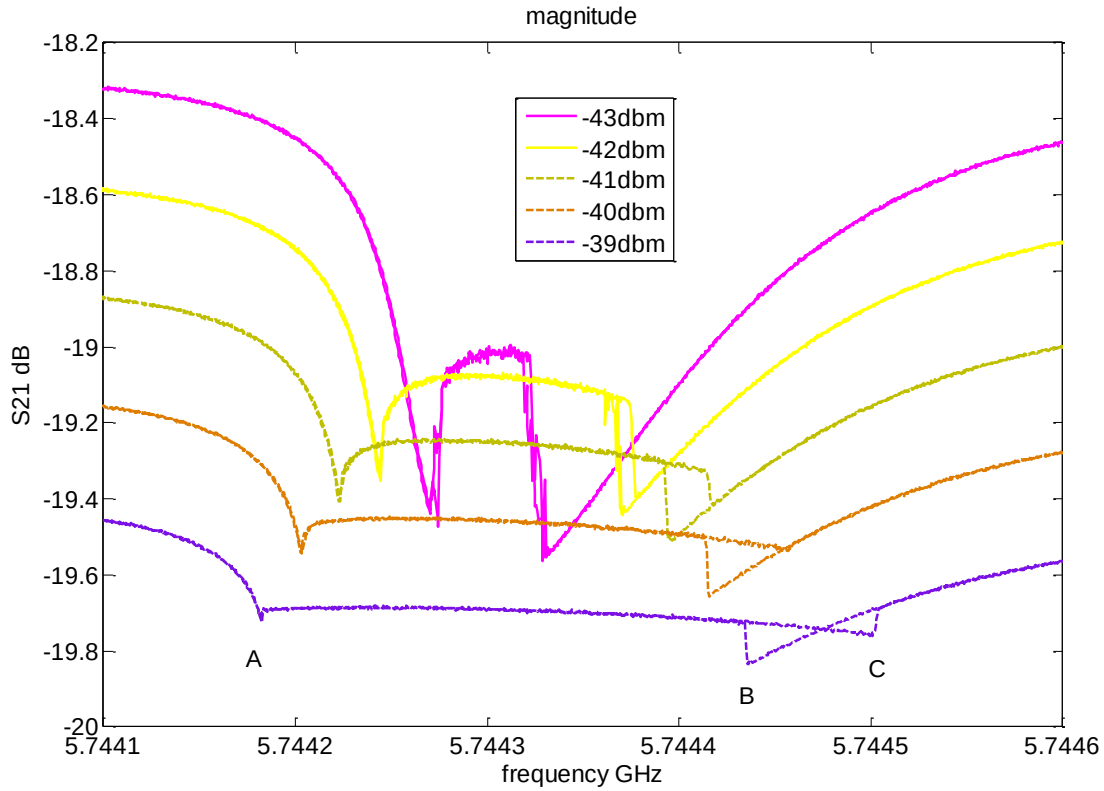
magnitude
-43dbm
-42dbm
-41dbm
-40dbm
-39dbm
S21 dB
frequency GHz
A
B
C
-18.2
-18.4
-18.6
-18.8
-19
-19.2
-19.4
-19.6
-19.8
-20
5.7441
5.7442
5.7443
5.7444
5.7445
5.7446

(a)

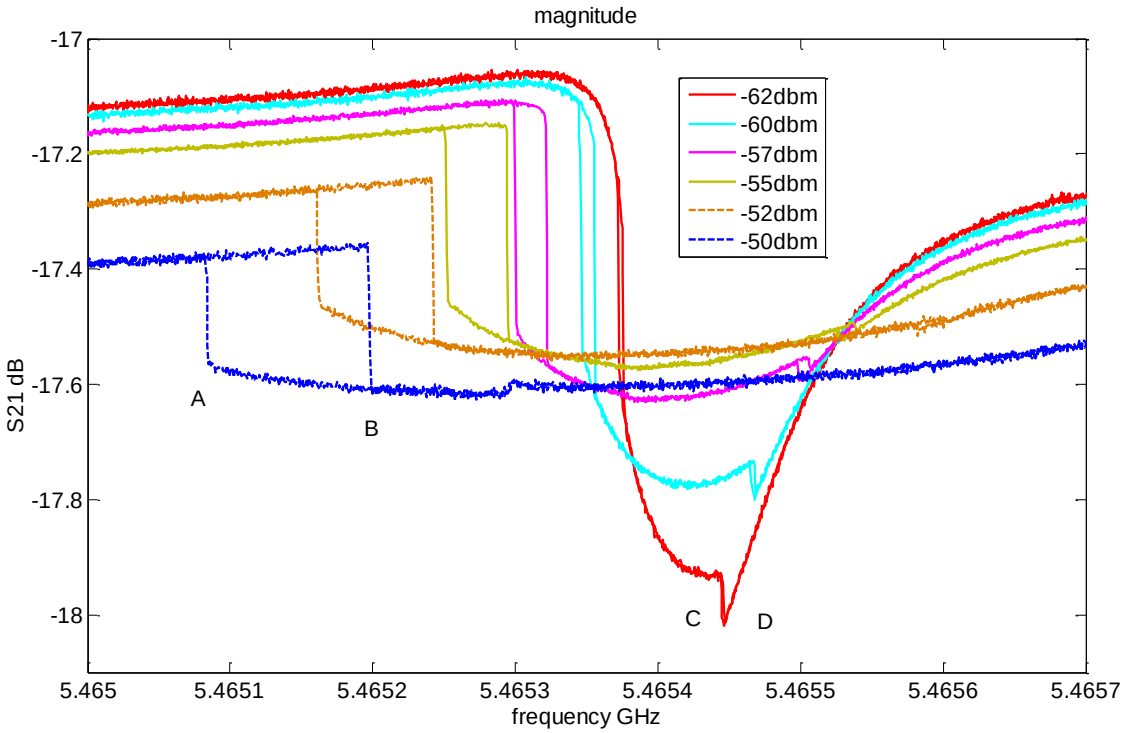
magnitude
-62dbm
-60dbm
-57dbm
-55dbm
-52dbm
-50dbm
S21 dB
frequency GHz
A
B
C
D
-17
-17.2
-17.4
-17.6
-17.8
-18
5.465
5.4651
5.4652
5.4653
5.4654
5.4655
5.4656
5.4657

(b)

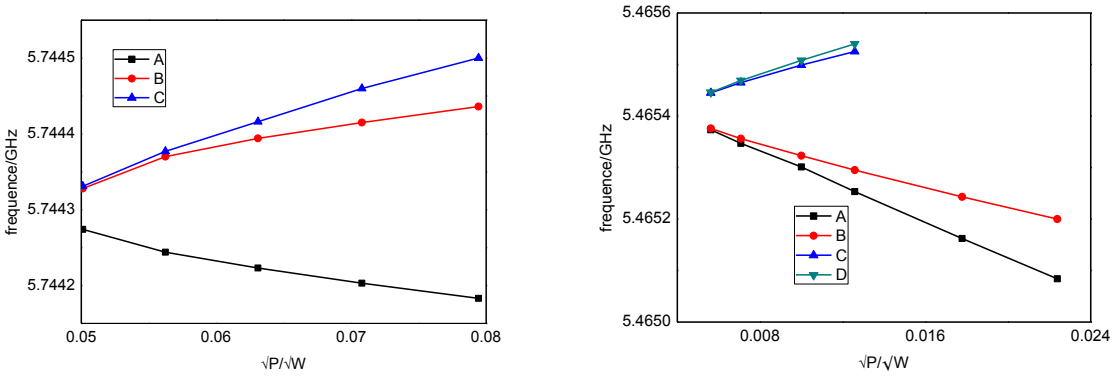

(c) (d)

Figure 7.5 (a) and (b) show bending of transmission curves when driving power increases, transmission versus frequency of peak #2 and peak #5 respectively of resonators with constrictions at 11mK at different driving powers. The positions of subpeaks of peak # 2 and peak # 5, (marked with A, B, C, D) as a function of square root of power are plotted on (c) and (d).

8

Conclusions and Outlook

This 7-month master thesis work will be concluded in this chapter. Based on this diploma project, a plan for the future work is outlined in this chapter also.

8.1 Conclusions

In summary, this diploma project started with simulations of resonators. Based on simulation results, we have designed and fabricated five resonators on one chip with resonance frequencies around 6 GHz and a wide range of external coupling. Constrictions of the central conductor in the middle of each resonator have been fabricated with electron beam lithography.

Transmission spectra of resonators with and without constrictions at resonance were measured at cryogenic temperatures. Power dependence and temperature dependence of each peak have been analyzed. Shift of resonance frequency as a function of temperature could be well explained by temperature dependence of kinetic inductance. When driving power increases, resonance shifts to lower frequency and Q decreases. When driving power is high enough, resonance curves show hysteretic behaviour because of nonlinear inductance.

Theoretical results deduced from lumped element model are in good agreement with measured data. By fitting theoretical formula to experimental curves, intrinsic parameters of

resonators, such as Qint and Ck, were calculated, and they are consistent with expected from design.

8.2 Future work

8.2.1 To characterise resonators with in-plane magnetic field

Usually, to achieve resonance between spins and cavity, magnetic field is needed to get suitable energy level splitting. Characterisation of resonators with in-plane magnetic field is crucial. Suppose zero-field splitting is zero, to tune the spin resonance frequency at 6GHz, magnetic field of 0.214T is needed according to $2B\mu_0 = hf$. If the applied current is 5A, diameter of superconducting cables is 0.127mm, 5 layers are needed for a solenoid coil. Based on these simple calculations, the design of superconducting coils for generating magnetic field is show in figure 8.1. To have more precise control of magnetic field, two assistant solenoids are put at sides of the main one.

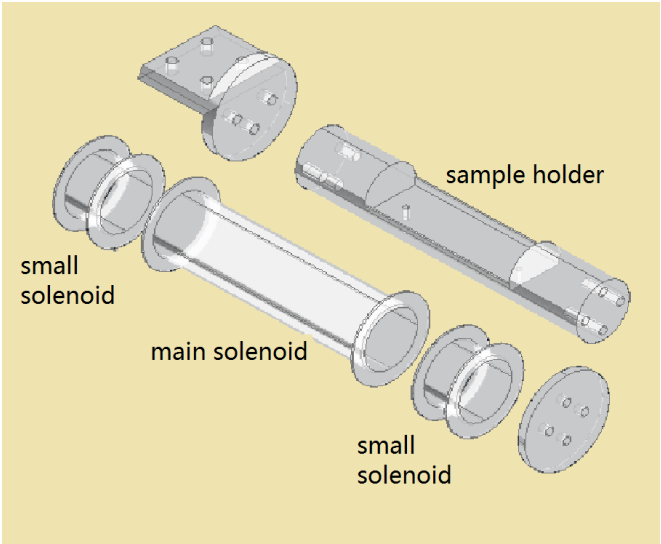

Figure 8.1 3D designs of superconducting coils for measurements of resonators with in-plane magnetic field.

8.2.2 To couple molecular spins to superconducting cavities

To realize a quantum spin memory, a more coherent electron-spin candidate is required. An ideal candidate would have a large zero-field splitting such that at $B = 0$, $\hbar\omega \gg k_b T$, which may come from crystal field splitting. Coupling of large ensembles of molecular spins to cavity modes will be done. The test molecules to be used are shown in figure 8.2

Cobalt(II) phthalocyanine Copper(II) phthalocyanine

Figure 8.2 Test molecules for spins to microwave photons coupling measurements

Appendix

Recipes for fabrication

1. Plasma etch to remove Al

Ar plasma – 10 sccm

Cl_2 plasma – 10 sccm

$SiCl_4$ plasma – 10 sccm

Power – 60 W RF

Time –3 minutes and 10 seconds

Pressure – 6 atmos

2. Plasma etch to remove Nb

CF_4 plasma – 60 sccm

O_2 – 3 sccm

Time – 3 minutes and 55 seconds

Power – 200 W DC, 30 W RF

Pressure – 20 atmos

Bibliography

[1] R. P. Feynman. *Simulating Physics with Computers.* International Journal of Theoretical Physics, 1982, 21: 467;

[2] P. Kaye, R. Laflamme, and M. Mosca. *An Introduction to Quantum Computing*, Oxford University Press, 2007;

[3] R. E. Slusher, L. Hollberg, B. Yurke, J. C. Mertz, and J. F. Valley. *Squeezed States in Optical Cavities: a Spontaneous-Emission-Noise Limit*. Physical Review A, 1985, 31(5): 3512;

[4] J.M. Raimond, P. Goy and S. Haroche, *Collective Interaction of Rydberg States with Microwave*, Applied Physics B, 1982, 29(3): 168;

[5] M. G. Raizen, R. J. Thompson, R. J. Brecha, H. J. Kimble, and H. J. Carmichael. *Normal-mode splitting and linewidth averaging for two-state atoms in an optical cavity,* Physical Review Letters, 1989, 63: 240;

[6] J. M. Fink, R. Bianchetti, M. Baur, M. Göppl, L. Steffen, S. Filipp, P. J. Leek, A. Blais, and A. Wallraff. *Dressed Collective Qubit States and the Tavis-Cummings Model in Circuit QED*, Physical Review Letters, 2009, 103: 083601;

[7] Y. Kaluzny, P. Goy, M. Gross, J. M. Raimond, and S. Haroche. *Observation of Self-Induced Rabi Oscillations in Two-Level Atoms Excited Inside a Resonant Cavity: The Ringing Regime of Superradiance*, 1983, 51: 1175;

[8] Y. Kubo, F. R. Ong, P. Bertet, D. Vion, V. Jacques, D. Zheng, A.Dréau, J-F. Roch, A. Auffeves, F. Jelezko, J. Wrachtrup, M. F.Barthe, P. Bergonzo, and D. Esteve. *Strong Coupling of a Spin Ensemble to a Superconducting Resonator,* Physical Review Letters, 2010, 105: 140502;

[9] D. I. Schuster, A. P. Sears, E. Ginossar, L. DiCarlo, L. Frunzio,J. J. L. Morton, H. Wu, G. A. D. Briggs, B. B. Buckley, D. D.Awschalom, and R. J. Schoelkopf,. *High-Cooperativity*

Coupling of Electron-Spin Ensembles to Superconducting Cavities, Physical Review Letters, 2010, 105: 140501;

[10] C. Gerry and P. Knight. *Introductory Quantum Optics*, Cambridge University Press, 2005;

[11] R. Schoelkopf and S. Girvin. *Wiring up Quantum Systems*, Nature, 2008, 451: 664;

[12] L. Frunzio, A. Wallraff, D. Schuster, J. Majer, and R. Schoelkopf. *Fabrication and characterization of superconducting circuit QED devices for quantum computation*. IEEE, Applied superconductivity, 2005, 15: 860;

[13] Barends, R. Baselmans, J.J.A. Hovenier, J.N. Gao, J.R. Yates, S.J.C. Klapwijk, T.M. Hoevers, H.F.C. Niobium and Tantalum High Q Resonators for Photon Detectors, IEEE, Applied superconductivity, 2007, 17: 263;

[14] A. D. O'Connell, M. Ansmann, R. C. Bialczak, M. Hofheinz, N. Katz, E. Lucero, C. McKenney, M. Neeley, H. Wang, E. M. Weig, A. N. Cleland,and J. M. Martinis. *Microwave dielectric loss at single photon energies and millikelvin temperatures*. Physical Review Letters, 2008, 92: 112903;

[15] M. Göppl, A. Fragner, M. Baur, R. Bianchetti, S. Filipp, J. M. Fink, P. J. Leek, G. Puebla, L. Steffen, and A. Wallraff. *Coplanar waveguide resonators for circuit quantum electrodynamics*. Journal of Applied Physics, 2008, 104: 113904;

[16] E A Tholén, A Ergül, K Stannigel, C Hutter and D B Haviland, *Parametric amplification with weak-link nonlinearity in superconducting microresonators*, Physica Scripta, 2009, T137: 014019;

[17] Holmes, P. J. and Rand, D. A., *The bifurcations of duffing's equation: An application of catastrophe theory*, Journal of Sound and Vibration, 1976, 44(2):237;